Distinct neocortical mechanisms underlie human SI responses to median nerve and laser evoked peripheral activation

Author names and affiliations:

Ryan V. Thorpe[a,†], Christopher J. Black[b], David A. Borton[b,c], Li Hu[d], Carl Y. Saab[a,b,e,*], Stephanie R. Jones[a,c]

[a]Department of Neuroscience, Brown University, Providence, RI, United States
[b]School of Engineering, Brown University, Providence, RI, United States
[c]Center for Neurorestoration and Neurotechnology, Providence VAMC, Providence, RI, United States
[d]Key Laboratory of Mental Health, Institute of Psychology, Chinese Academy of Sciences, Beijing 100101, China
[e]Department of Neurosurgery, Rhode Island Hospital, Providence, RI, United States
*Present address: Department of Biomedical Engineering, Lerner Research Institute, Cleveland Clinic, Cleveland, OH, United States; Department of Biomedical Engineering, Case Western Reserve University, Cleveland, OH, United States
[†]Corresponding author

Abstract

Magneto- and/or electro-encephalography (M/EEG) are non-invasive clinically-relevant tools that have long been used to measure electromagnetic fields in somatosensory cortex evoked by non-painful and painful somatosensory stimuli. Two commonly applied stimulation paradigms that produce distinct responses in primary somatosensory cortex (SI) linked to non-painful and painful sensations are electrical median nerve (MN) stimulation and cutaneous laser-evoked (LE) stimulation to the dorsum of the hand, respectively. Despite their prevalence, the physiological mechanisms that produce stereotypic macroscale MN and LE responses have yet to be fully articulated, limiting their utility in understanding brain dynamics associated with non-painful or painful somatosensation. We examined the neocortical circuit mechanisms contributing to MN and LE responses in SI using the Human Neocortical Neurosolver (HNN) neural modeling software tool. HNN was specifically designed for biophysically principled interpretation of the cell and circuit origin of M/EEG signals (Neymotin et al., 2020). Detailed analysis of the timing and orientation of peaks in source localized SI current dipole responses from MN and laser-evoked (LE) stimulation showed that these features were robust and conserved across prior studies. The first peak in the MN response at ~20 ms corresponds to outward-directed deep-to-superficial electrical current flow through the cortical laminae, while the initial LE response occurs later at ~170 ms and is oriented in the opposite direction. Historically, these peaks have both been labeled N20 and N1, despite their opposite current orientations. Simulating the cellular and circuit-level mechanisms accounting for these and later peaks with HNN's detailed laminar neocortical column model revealed that the MN response can be simulated with a sequence of layer-specific exogenous excitatory feedforward and feedback synaptic drive. This sequence was similar to that previously reported for tactile evoked responses (Jones et al., 2007; Neymotin et al., 2020), with the novel discovery of an early excitatory feedback input to superficial layers at ~30 ms post-stimulus that facilitated generation of the MN response's first prominent inward-oriented deflection, known historically as the P30. Simulations of the LE response revealed that the initial ~170 ms inward-deflection required a burst of repetitive gamma-frequency (~40 Hz) excitatory supragranular feedback drives, consistent with prior reports of LE gamma-frequency activity. These results make novel and detailed multiscale predictions about the dynamic laminar circuit mechanisms underlying temporal and spectral features of MN and LE responses in SI, and can guide further investigations in follow-up studies. Ultimately, these findings may help with the development of targeted therapeutics for pathological somatosensation, such as chronic and neuropathic pain.

1. Introduction

Somatosensation is a crucial mechanism for healthy human behavior and survival that is often segregated into two categories: non-painful (for example gentle touch or peripheral nerve stimulation) and painful (for example unpleasant heat) sensations. The distinct neural receptors and pathways mediating innocuous and noxious somatosensory signals to the brain have been well categorized (Almeida et al., 2004; Burke et al., 1975; Lamour et al., 1983; Treede et al., 1999; Willis, 2007, 1985). However, how these signals are uniquely processed within brain circuits to generate reciprocal sensations of innocuous, non-nociceptive somatosensation *versus* noxious, nociceptive somatosensation is not well understood. The brain's electrophysiological correlates of somatosensation can be readily studied non-invasively in humans using electro- and/or magneto-encephalography (M/EEG), which reflects fast-time scale neural signals from neocortex. Numerous studies have identified unique and robust M/EEG-measured evoked responses to non-painful and painful somatosensory stimuli, yet, little is known of the dynamic, multiscale neocortical circuits that produce these perceptually distinct evoked responses.

Two peripheral stimulation paradigms stand out in the literature as producing distinct responses in primary somatosensory cortex (SI) linked to non-painful and painful sensations: electrical median nerve (MN) stimulation and cutaneous laser-evoked (LE) stimulation to the dorsum of the hand, respectively. Although MN and laser stimuli are not naturalistic sensory stimuli, uncovering the underlying neural process they induce can provide a foundation for understanding how the brain differentially processes non-painful *versus* painful sensations in general. MN stimulation and more broadly tactile stimulation of the hand evokes its earliest electrophysiological response in contralateral SI, specifically area 3b/1, at ~20 ms (Cauller and Kulics, 1991; Huttunen et al., 2006; Kanno et al., 2003; Lin et al., 2005, 2003; Lipton et al., 2006; Schroeder et al., 1995; Tiihonen et al., 1989; Wikström et al., 1996). Laser stimulation of the hand evokes a later response in a topographically similar region of contralateral SI at ~170 ms (Christmann et al., 2007; Jin et al., 2018; Kakigi et al., 2005; Ploner et al., 1999; Timmermann et al., 2001; Valentini et al., 2012). While different sub-second time-domain components (e.g., peak amplitudes) of the MN response and LE response in SI appear to aid in encoding the location (Cauller and Kulics, 1991; Ishibashi et al., 2000; Omori et al., 2013; Schroeder et al., 1995), strength, and perceived intensity (Lin et al., 2003; Timmermann et al., 2001) of the sensory stimulus, the precise neural mechanisms that facilitate such an encoding remain unknown. While prior studies have hypothesized that specific sequences of excitatory (EPSC) or inhibitory (IPSC) postsynaptic currents on targeted cells in the laminar neocortex contribute to somatosensory evoked responses (Kenshalo et al., 2000; Whitsel et al., 2010; Wikström et al., 1996), the direct influence of such mechanisms to recorded macroscale M/EEG responses has yet to be demonstrated.

This study addresses the challenge of predicting circuit mechanisms from M/EEG-measured MN and LE signals through biophysically detailed neural modeling using Human Neocortical Neurosolver (HNN)

(Neymotin et al., 2020)). In brief, HNN is a user-friendly software tool that simulates the primary electrical currents responsible for generating M/EEG signals in a biophysically-principled laminar neocortex model. HNN has been used to study circuit mechanisms of innocuous tactile stimulation and correlates of tactile perception in SI measured with MEG and EEG (Jones et al., 2009, 2007; Law et al., 2021; Neymotin et al., 2020; Sliva et al., 2018; Ziegler et al., 2010). Consistent with prior literature and invasive recordings, HNN simulations showed that the tactile evoked (TE) response from a brief tap to the contralateral middle finger tip is generated by a sequence of layer specific excitatory synaptic drives to the SI circuit. Here we extended these prior studies to investigate mechanisms of electrically stimulated median nerve responses from M/EEG data source localized to SI, which have unique features when compared to TE responses.

We also identified distinct components of the MN response (Jones et al., 2007; Kanno et al., 2003; Lenoir et al., 2017; Lin et al., 2005, 2003; Tiihonen et al., 1989; Wikström et al., 1996) compared with the LE response (Baumgärtner et al., 2011; Jin et al., 2018; Lenoir et al., 2017; Omori et al., 2013; Ploner et al., 1999; Raij et al., 2003; Schlereth et al., 2003; Valentini et al., 2012), as reported in prior studies. Given that sensations evoked by MN and laser stimuli are perceptually distinct, as are their electrophysiological signatures, we hypothesized that their corresponding evoked responses in SI are generated through distinct physiological mechanisms of a common underlying neocortical circuit. Our HNN SI modeling led to novel predictions on the neural mechanisms underlying each response within the HNN SI model.

Overall, close consistency between the modeled and recorded data suggests that distinct features of the MN and LE responses emerge from differences in the temporal and spectral profiles of exogenous layer-specific excitatory synaptic drive to the SI circuit. The detailed model predictions provide several targets for further validation with invasive recordings or other imaging modalities and can serve as the baseline for future studies of non-painful and painful somatosensation.

2. Materials and Methods

2.1. Median Nerve Evoked Response Data

The first part of our HNN examination focused on interpreting the trial-averaged (n=1 healthy male human participant, age 39; 111 trials) contralateral MN response in the right hemisphere of a representative human participant (Figure 1a). This dataset was originally published in Sorrentino et al., 2009 and is publicly available with MNE-Python (Gramfort et al., 2014; https://mne.tools/stable/overview/datasets_index.html#somatosensory). The dataset measures the MEG response to electrical median nerve stimulation of the left wrist at the motor threshold with a uniformly random-sampled interstimulus interval between 7.0 and 9.0 s, as described in the original study, and was collected with written informed consent from the participant and prior approval from the local ethics committee (Sorrentino et al., 2009).

Given conflicting results in the literature regarding the true number of current dipole sources in and around SI that contribute to the sensor-level evoked response of transcutaneous electrical stimulation of the hand (Ishibashi et al., 2000) and/or median nerve (Huttunen et al., 2006; Lin et al., 2005, 2003; Peterson et al., 1995; Tiihonen et al., 1989; Wikström et al., 1996), we adopted an approach for source-localizing the MN response that made no a priori assumption about the number of true generators. Using MNE-Python (Gramfort et al., 2013), we fitted a distributed inverse solution by calculating the noise-normalized (i.e., the dynamic statistical parametric mapping [dSPM]) minimum norm estimate inverse solution, selected the vertex with maximal cumulative activation over the first 40 ms time window, and finally extracted the time course of the selected vertex (see Figure 1a) from the non-noise-corrected minimum norm estimate (MNE). While this method differs from other methods that fit an equivalent current dipole (ECD) or estimate an average response in a highly active region-of-interest (ROI), our selected vertex represents dipolar current flow constrained to a small, highly responsive region of the neocortex.

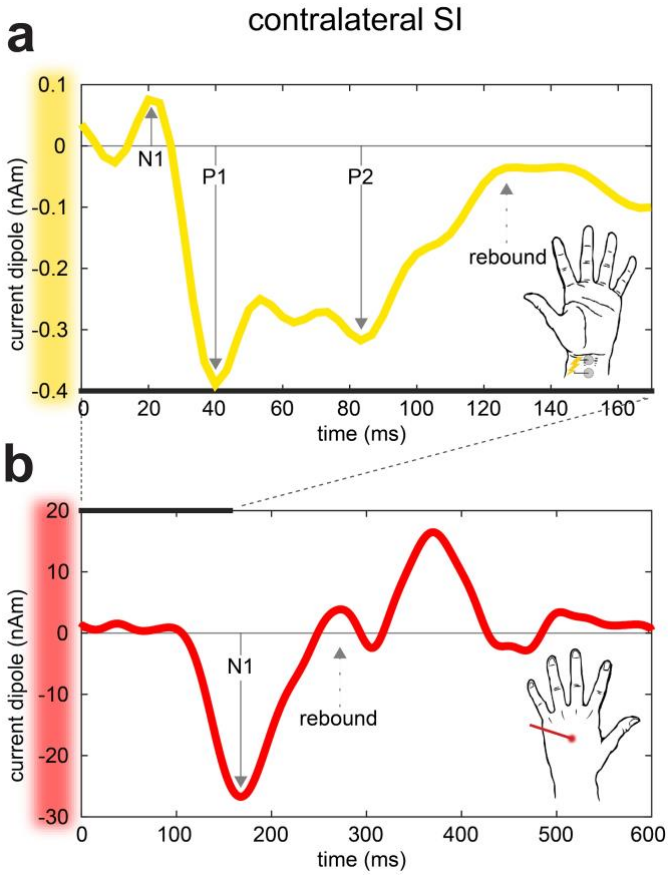

Figure 1. Contralateral SI produces two distinct evoked responses to MN and laser stimulations. While the representative MN response (average response for one subject across 111 trials) in (a) and representative LE response (average response for n=107 subjects across 80 trials/subject) in (b) appear to exhibit fundamental differences in magnitude and duration, this study aims to determine the minimal sequence of distinct synaptic perturbations required for a local SI circuit to produce either the MN response (consisting of N1, P1, and P2 deflections followed by a rebound) or LE response (consisting of an N1 deflection followed a by a rebound) independent of scale.

We also extracted three additional MN response waveforms from prior publications to demonstrate the primary waveform features of the MN response analyzed in this study (i.e., as identified in the previous paragraph) in the context of previous work. Namely, we used the WebPlotDigitizer application (https://automeris.io/WebPlotDigitizer/) to extract and reproduce the time course from an MEG source-space MN response of a single subject (Lin et al., 2003). Permission for reproduction will be obtained upon publication. Furthermore, we reproduced the group-averaged MEG source-space suprathreshold TE response from a brief tap to the contralateral middle finger tip (Jones et al., 2007) that was supplied alongside the HNN software, and we used the EEG dataset from Lenoir et al., 2017, as provided by its authors, to compute the average sensor-space MN response potential at contralateral parietal electrodes (i.e., P3 or P4) referenced to Fz. For the purpose of waveform comparison (i.e., when plotting them on the same axes), each time course was normalized by the standard deviation of the signal across time (Figure 4a). See 3.1 for a discussion of the commonalities in the SI MN responses across studies that we focused on interpreting with our HNN model.

2.2. Laser Evoked Response Data

The second part of our HNN examination focused on interpreting the group-averaged (n=107 healthy human participants ages 18-26, 67 of which were female; 80 trials/participant) contralateral LE response computed from ECD modeling that was published in a prior study (Jin et al., 2018). All human participants associated with this dataset provided written informed consent and the experimental procedures were approved by the local ethics committee. As outlined by Jin and colleagues, laser stimulus was applied 40 times to the dorsum of the left and right hands of each participant with a uniformly random-sampled interstimulus interval between 11 and 15 s, and whose laser-beam target was shifted ~1 cm after each stimulus to avoid overheating of the skin and nociceptor fatigue or sensitization. The energy level of each stimulus was randomly sampled from four values that corresponded to subjective pain ratings of ~2, ~4, ~6, ~8 on a 0-10 numerical rating scale. The contralateral SI ECD to the left or right hand was fitted to EEG scalp topography as part of a four-dipole model (Jin et al., 2018). Here, we averaged the SI response across hemispheres to calculate the cumulative mean EEG evoked response to cutaneous laser stimulation applied to either hand (Figure 1b).

We also extracted additional LE response waveforms from prior publications (Figure 4b). We used the WebPlotDigitizer application to extract and reproduce the LE response of an MEG source-space response from a single subject (Raij et al., 2003) and an EEG source-space group average response (Schlereth et al., 2003). Permission for reproduction will be obtained upon publication. The EEG dataset from (Lenoir et al., 2017) was provided by the authors, and used to compute the average sensor-space LE response at contralateral central electrodes (i.e., C3 or C4) referenced to Fz. When plotted on the same axes as other LE response waveforms, each time course was normalized by the standard deviation of the signal across

time (Figure 4b). See 3.1 for a discussion of the commonalities in the SI LE responses across studies that we focussed on interpreting with our HNN model.

Unless specified otherwise, all further mentions of the MN or LE response refer to the representative current dipole moments presented in Figure 1.

2.3. HNN Computational Neural Modeling

The HNN software was designed for cellular and circuit level interpretation of source localized human MEG/EEG signals (Neymotin et al., 2020). The core of HNN is a detailed model of a laminated cortical circuit under thalamocortical and cortico-cortical influences that simulates the primary electrical currents generating M/EEG signals from a localized patch of the cortex (Figure 2). HNN's model was designed to include canonical features of cortical circuitry, including synaptically connected pyramidal neurons and interneurons in supragranular and infragranular layers, and layer specific feedforward and feedback synaptic drive. HNN simulates the primary current sources of M/EEG from the net intracellular current flow across the pyramidal neuron populations in the model, based on the established biophysical origin of these currents (Hämäläinen et al., 1993; Murakami and Okada, 2006; Næss et al., 2021; Okada et al., 1997). In practice, users define patterns of action potentials representing activity in exogenous networks (e.g., thalamus or higher order cortex) that drive the local network through layer specific patterns of excitatory synaptic inputs. Synaptic inputs that drive the network target the dendrites of excitatory pyramidal cells and the somas of inhibitory basket cells. One pathway of input simulates perturbations ascending from the peripheral nervous system, through the lemniscal thalamus to the granular layers (L4), and finally propagating to the proximal dendrites of the pyramidal neurons in supra- and infragranular layers. These inputs are referred to as proximal drive and represent "feedforward" activation of the circuit. The other pathway of input comes from the non-lemniscal thalamus or high-order cortex and synapses in the supragranular layers, targeting the distal dendrites of the pyramidal neurons. These inputs are referred to as distal drive and can represent "feedback" activation of the circuit (Neymotin et al., 2020). Note that the HNN model represents synaptic weight as the maximal conductance associated with a given receptor's IPSC or EPSC. Pyramidal neurons provide both fast and slow AMPA/NMDA-mediated excitation, and inhibitory neurons provide both fast and slow $GABA_A$/$GABA_B$-mediated inhibition.

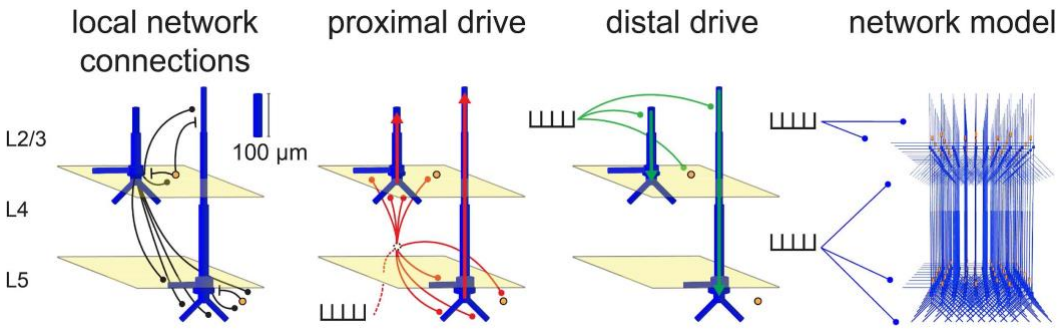

Figure 2. HNN leverages cellular and circuit-level structure to model the primary current flow up and down the long apical dendrites of pyramidal neurons. Local network connections (black) bridge excitatory pyramidal cells (blue) with inhibitory basket cells (yellow circles) and each other. Proximal inputs (red) arrive as feedforward excitatory drive from the lemniscal thalamus and target the granular layer (L4; middle) that propagate directly to the proximal dendrites of the pyramidal neurons in supragranular (L2/3; top) and deep layers (L5; bottom). The initial circuit response of a proximal drive is to push current up the apical dendrites of pyramidal cells. Distal inputs (green) arrive as feedback excitatory drive from the non-lemniscal thalamus or high-order cortex and target the distal portion of the apical dendrite in the supragranular layer. The initial circuit response of a distal drive is to push current down the apical dendrites of pyramidal cells. Inhibitory drive to the circuit and other more complex interactions result from the spatiotemporal dynamics that emerge from basket cell activation. The canonical model network is composed of 35 L2/3 basket cells, 35 L5 basket cells and a 10x10 grid of L2/3 and L5 pyramidal cell pairs that are connected across the grid according to type with exponential synaptic weight fall-off. Adapted from (Neymotin et al., 2020).

While numerous parameters influence the response of the model's high-dimensional dynamical system, any simulation begins by defining the type, strength, and relative timing of driving inputs (i.e., action potentials), which are chosen to reflect the experimental conditions and initial hypotheses. Here, the initial pattern of drive to simulate the ME response is motivated by our prior studies simulating SI tactile evoked responses (Jones et al., 2009, 2007; Neymotin et al., 2020; Sliva et al., 2018; Ziegler et al., 2010), as detailed below. Multiple trials are simulated and variance is built into each simulation by jittering the timing and distribution of the driving spikes on each trial, which have mean and variance defined by Gaussian distributions. Note that all drives in the present study were synchronously applied to all cells (i.e., one spike time was sampled to supply an excitatory synaptic input to all cells in the network for each drive of a given trial). Parameter values defining the exogenous inputs to the network are provided in the Results section.

The aggregate current dipole was computed by summing the intracellular currents in all pyramidal neurons across both L2/3 and L5 flowing in a direction parallel to the apical dendrites (Neymotin et al., 2020). The units of measures of the simulated dipole current are nano-Ampere-meter and are directly comparable to the source localized data in equal units. Microcircuit activity, such as cell spiking profiles, can also be visualized leading to detailed predictions on the circuit mechanisms inducing the recorded macroscale current dipole signal.

Further details on the HNN model can be found in the methods publication (Neymotin et al., 2020). Open-source code for the HNN model and its graphical user interface are provided online at https://github.com/jonescompneurolab/hnn and corresponding tutorials at https://hnn.brown.edu. The specific parameter files used here will be distributed upon publication.

2.4. Processes for tuning parameters to fit recorded data

Using the HNN graphical user interface, we defined a sequence of proximal and distal inputs and fitted the parameters representing these drives to reproduce close agreement to primary waveform features of the empirical MN and LE responses. Specifically, we modulated the type, relative timing, and strength (i.e. maximal conductance) of driving inputs in order to determine the minimal sequence of distinct synaptic perturbations required for a local SI circuit to differentially produce either the MN or LE waveform as presented in Figure 1. To account for the relative difference in magnitude between the MN and LE responses, a scaling factor is applied to all simulated dipoles that aligns the magnitudes of simulated and empirical evoked responses, since the model is a reduced representation of the larger networks contributing to the response.

We first used manual tuning to add or remove proximal and distal inputs to/from the model and determined the scaling factor for each waveform that by visual inspection created a close approximation to the recorded data. Manual tuning was also used to determine a local network configuration that would prevent runaway firing given the number and types of evoked inputs (see Table 1, note that the same local configuration was used for MN and LE responses). We refer to the set of parameters arrived at from manual tuning as the pre-optimization parameter set (pre-OPS).

After the initial manual tuning, we used the non-linear numerical optimization routine built into HNN to 1) refine the fit of the simulation across evoked input parameters and 2) demonstrate that a local minimum in the root mean squared error (RMSE) between the simulated and recorded waveforms has been reached (Neymotin et al., 2020). Optimization routines were configured to explore all exogenous proximal and distal drive-related parameters of the pre-OPS and run 3 iterations per parameter in each optimization stage (see Figures 6, 8, and 10 for the parameter list). Each iteration consisted of a full simulation (i.e., with n=100 trials, 170 and 300 ms/trial for the MN and LE responses, respectively) except for any LE response pre-OPS with 5 or more drives, which given its computational cost, consisted of a 50-trial simulation to reduce run-time.

Target:	**L2/3 Pyramidal**	**L5 Pyramidal**	**L2/3 Basket**	**L5 Basket**
Source:				
L2/3 Pyramidal	AMPA: 2e-4* NMDA: 2e-4*	AMPA: 2e-4* NMDA: n/a	AMPA: 5e-4 NMDA: n/a	AMPA: 2.5e-4 NMDA: n/a
L5 Pyramidal	n/a	AMPA: 1e-3* NMDA: 5e-4	n/a	AMPA: 5e-4 NMDA: n/a
L2/3 Basket	$GABA_A$: 5e-2 $GABA_B$: 5e-2	$GABA_A$: 2e-3* $GABA_B$: n/a	$GABA_A$: 2e-2 $GABA_B$: n/a	n/a
L5 Basket	n/a	$GABA_A$: 2e-2* $GABA_B$: 6e-2*	n/a	$GABA_A$: 2e-2 $GABA_B$: n/a

Table 1. Local network parameters of the computational model. Each value represents a synaptic weight (μS) for an excitatory (i.e., AMPA or NMDA) or inhibitory (i.e., $GABA_A$ or $GABA_B$) connection. Asterisks denote parameters that were initially tuned from the default values distributed with HNN to prevent runaway network excitability and then left constant for all simulations presented in the results of this study.

All stages of manual tuning and optimization were conducted with a small dipole smoothing window width of 5 ms, to minimize high frequency variance induced by spiking in the simulated network, which we assume averages out in the larger network contributing to the recorded data. Correspondingly, all manually-tuned pre-optimization simulations addressed in the results (with the exception of Figure 5a) reflect dipoles with minimal smoothing (i.e., with a 5 ms-wide Hamming window). All other simulations that have been through parameter optimization show a greater amount of smoothing (i.e., with a 20 ms-wide Hamming window) to reflect final-product dipoles that are more consistent with the smoothing convention established in parameter sets distributed with the HNN software (Neymotin et al., 2020).

2.5. Simulation statistics and goodness-of-fit

Variability is built into each HNN simulation trial through variance in the timing of the spikes that activate the network through proximal and distal projection patterns on a given trial, as described above. HNN samples the trial-specific spike time of a given proximal or distal drive from a normal distribution according to user-defined mean and standard deviation (Jones et al., 2007; Neymotin et al., 2020). Correspondingly, each simulation in this study produced a current dipole waveform for each trial and for the trial-mean (n=100 trials). For a goodness-of-fit statistic, we calculated RMSE between the empirical current dipole and simulated trial-mean current dipole.

2.6. Time-frequency response

The average time-frequency response (TFR) was calculated from 3-100 Hz across simulated aggregate current dipole trials by computing each trial's TFR through convolution of the zero-padded time course with an *m*=*f*/3 cycle Morlet wavelet of the form $w(t,f)=A\cdot \exp\left(\frac{-t^2}{2\sigma^2}\right)\cdot \exp(i2\pi ft)$, where $A=\left(\frac{1}{2}\sum_{t}|w(t,f)|^2\right)^{-1/2}$ and $\sigma=\frac{m}{2\pi f}$ for a given frequency value *f*. To preserve high-frequency components and minimize edge effects in the TFR calculation of each time course, trials were smoothed with a 5 ms-wide Hamming window and run for a longer length of time for a total of 600 ms. TFR trials were then cropped at t=300 ms. Given that the TFR was only calculated for the LE response simulations which maintained a current dipole close to zero for the first ~100 ms, edge effects at the beginning of each time course were negligible.

3. Results

3.1. MN and LE responses have distinct temporal profiles and early peaks representing current flow in opposite directions across the cortical layers

The representative trial-averaged evoked responses analyzed with HNN in this study (Figure 1) were selected because they embody waveform features that are broadly consistent across subjects, experimental conditions, and M/EEG imaging modalities (see Table 2, Table 3, and Figure 4 for a comparison of these waveforms across MN and LE responses published in prior studies). The MN response (see Figure 1a and Figure 4a) is fast and the majority of its activity occurs from 20-130 ms post-stimulus with three distinct deflections: MN N1, P1, and P2. (Also note the small rebound at 50-70 ms [MN N2], which in some studies is prominent enough to be labeled as its own distinct deflection.) The LE response (see Figure 1b and Figure 4b) emerges more slowly and the majority of its activity occurs from 100-450 ms with one primary deflection (LE N1) followed by two small rebound peaks. Here, the magnitude and latency of the LE response are both significantly greater than for the MN response, due in part to disparate stimulation intensities, different source localization techniques applied to each dataset (see Methods) and different latencies (i.e., early latency evoked responses tend to be smaller than greater latency evoked responses).

The orientation of each SI response in Figure 1 has been aligned so that positive deflections correspond to dipole currents oriented from deep to superficial layers (i.e., out of the cortex) while negative deflections correspond to currents from superficial to deep layers (i.e., into the cortex). A more detailed description of how the current direction was determined, and how it relates to interpreting the circuit mechanisms with HNN, is given below. With the alignment as specified above, the MN response begins with a small upward deflection (MN N1) at ~20 ms followed quickly by a large downward P1 deflection at ~40 ms. The "negative" labeling of the MN N1 deflection comes from the fact that it corresponds to a current sink in the

posterior (referenced to anterior) cortex as measured from EEG sensors. More specifically, the earliest electrical field of somatosensory evoked potentials at the posterior sensor minus anterior sensor is negative (Deiber et al. 1986). This nomenclature has also been adopted in MEG. Using the polarity-latency nomenclature, the MN N1 has historically been referred to as N20 (Deiber et al., 1986; Tiihonen et al., 1989). The LE response begins with a large downward deflection (LE N1) at ~170 ms followed by two smaller rebound peaks. Of note, in (Jin et al., 2018) the LE N1 in SI is shown with positive polarity, however the current is oriented into the cortex at this peak, and as such is flipped to have a negative value in Figure 1.

To demonstrate how fixed dipole inverse methods (such as those used to produce the MN and LE responses in this study) can be applied to determine the orientation of the SI current dipole in or out of the cortex at a given peak, we detail the first two deflections of the MN case. Figure 3a shows the location and absolute magnitude of the initial response from MN stimulation averaged over the first 40 ms, and Figure 3b shows the dipole moment time course at the vertex of peak activation. Figure 3c displays the orientation and forward (i.e., posterior-to-anterior) direction of the dipole moment at the MN N1 (20 ms) at this vertex, which reflects current flow traveling from deep to superficial layers (out of the cortex). Conversely, the MN P1 (40 ms), reflects backward (i.e., anterior-to-posterior) current flow traveling from superficial to deep layers (into the cortex, Figure 3d). The cross-sectional cut-out of the central sulcus (CS) and postcentral gyrus rendered in Figure 3e illustrates how the inferred laminar orientation of a dipole moment deflection depends on the dipole's location within the folds of SI. See Table 2 for a summary of the MN response dipole's mesoscopic direction and inferred laminar orientation at its N1 deflection in prior publications. At the circuit level, outward currents (positive deflections) correspond to current flow up the cortical pyramidal neuron apical dendrites, while inward currents (negative deflections) correspond to currents down the pyramidal neuron apical dendrites, as will be studied further below with HNN.

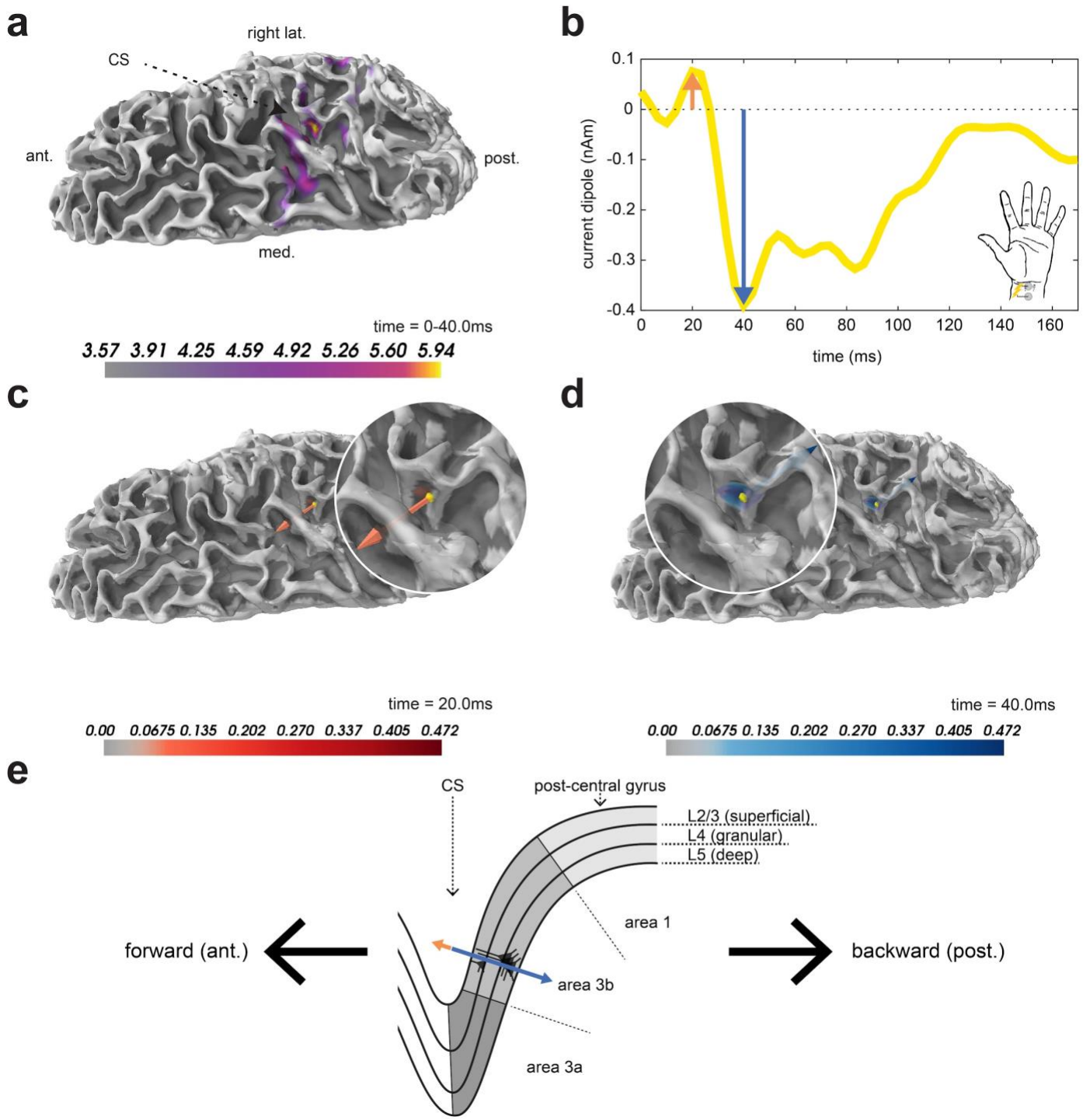

Figure 3. Waveform deflections in M/EEG source-space correspond to sequential, orientation-specific activation of a contralateral median nerve-responsive cortical dipole. (a) Dorsal view of the right hemisphere's average dynamic statistical parametric map (dSPM) of the minimum norm estimate (MNE) over the first 40 ms post-stimulation. To isolate a vertex-of-interest (VOI), the single most active early-latency vertex was selected from the dSPM and shown in yellow. Note that maximal dSPM activity occurs in the hand representation of area 3b on the posterior wall of the central sulcus (CS). (b) The MN response found by selecting the MNE time course at the VOI. (c) Direction and orientation of the current dipole at 20.0 ms. (d) Same as in (c), except at 40.0 ms. (d) Cartoon schematic demonstrating how the location and mesoscopic direction of the current dipole correspond to laminar orientation and direction at each deflection of the dipole time course. The first major deflection of the MN response at 20.0 ms represents forward current flow oriented *out* of the cortex (i.e., from deep to superficial layers). The second major deflection at 40.0 ms represents backward current flow oriented *into* the cortex (i.e., from superficial to deep layers).

Direction and inferred laminar orientation of the MN response dipole at its N1 deflection in prior publications						
Publication	**Measurement modality**	**Group-level/single subj. dipole fit**	**Peak time (mean ±SEM)**	**Dipole location (Brodmann area)**	**Primary dipole direction**	**Inferred laminar dipole orientation**
Jones et al., 2007*†	MEG	Single (n=7)	LH: 23.3	3b	forward	outward
Kanno et al., 2003	MEG	Single (n=14)	19.8±0.2	3b	forward	outward
Lin et al., 2003*	MEG	Single (n=13)	RH: 21.7±0.4	3b	forward	outward
Lin et al., 2005	MEG	Single (n=17)	RH: 22.1±0.2	3b	forward	outward
Tiihonen et al., 1989	MEG	Single (n=6)	RH: 19.7±1.8 (mean±SD)	3b	forward	outward
Wikstrom et al., 1996	MEG	Single (n=9)	RH: 21.0±1.6 (mean±SD)	3b	forward	outward

Tabel 2. Directionality of the contralateral SI dipole current from MN stimulation at the time of the N1 deflection in prior publications. The stimulus was applied to the median nerve of the hand and its evoked response measured in the relative contralateral hemisphere of the cortex. *A representative evoked response waveform from this study is reproduced in Figure 4a. †This study delivered tactile stimulation to the first digit of the hand rather than median nerve stimulation. Left hemisphere, LH; right hemisphere, RH; standard error of the mean, SEM; standard deviation, SD.

Similar to the MN response, the LE response localizes to a region in and around area 3b of the hand representation in SI. However, its first primary deflection (i.e., the LE N1) represents current flowing from superficial to deep layers (i.e., into the cortex; see the literature review in Table 3). There is some variability across experiments regarding the exact area in SI that is primarily responsible for producing the LE response observed in M/EEG recordings, with studies citing area 3a in the CS, area 3b on the postcentral wall of the CS, area 1 on the crown of the postcentral gyrus, or area 2 on the anterior wall of the postcentral gyrus (Table 3). The majority of prior studies indicate that the LE N1 localizes to area 3b/1 and is either oriented backward (anterior-to-posterior) when localized more toward the anterior wall of the

postcentral gyrus or oriented downward when localized more toward the crown of the postcentral gyrus (Table 3). Localization in 3b/1 is also supported by invasive recordings in non-human primates that identified pyramidal neurons nearer to area 1 (at the crown of the postcentral gyrus) as being the primary target of nociceptive projections to SI (Kenshalo et al., 2000; Vierck et al., 2013).

Direction and inferred laminar orientation of the LE response dipole at its N1 deflection in prior publications						
Publication	**Measurement modality**	**Group-level/single subj. dipole fit**	**Peak time (mean ±SEM)**	**Dipole location (Brodmann area)**	**Primary dipole direction**	**Inferred laminar dipole orientation**
Baumgärtner et al., 2011	intracranial EEG grid	Single (n=2)	LH: 138 RH: 141	3a/3b	backward	inward
Jin et al., 2018*	EEG	Group (n=107)	LH: 165 RH: 170	non-specific SI	downward/ forward	inward
Omori et al., 2013†	MEG	Single (n=4)	RH: 169±12	3b/1	backward	inward
Ploner et al., 1999	MEG	Single (n=6)	174±3	3b/1	backward	inward
Raij et al., 2003*	MEG	Single (n=8)	RH: 160-195	non-specific SI	backward	inconclusive
Schlereth et al., 2003*	EEG	Single (n=10)	180±7	1/2	backward	outward
Valentini et al., 2012	EEG	Group and single (n=35)	LH: 156 RH: 157	non-specific SI	downward/ forward	inward

Tabel 3. Directionality of the contralateral SI dipole current from laser stimulation at the time of the N1 deflection in prior publications. The stimulus was applied to the dorsum of the hand and its evoked response measured in the relative contralateral hemisphere of the cortex. *A representative evoked response waveform from this study is reproduced in Figure 4b. †This study delivered noxious intraepidermal electrical stimulation to the dorsum of the hand rather than cutaneous laser stimulation. LH, left hemisphere; RH, right hemisphere; standard error of the mean, SEM.

The primary features of the MN and LE response waveforms in Figure 1 are consistent when applying several different inverse solution methods, and are conserved across MEG and EEG recording modalities

and experimental tasks (see Figure 4). Note that while the exact timing of each peak in the amplitude-normalized responses in Figure 4 are reproduced from various prior studies and hence vary slightly, each waveform is oriented such that the first major N1 deflection points in the positive direction for the MN response (Figure 4a) and in the negative direction for the LE response (Figure 4b). In Figure 4a, we see that the MN N1 is followed sequentially by three more peaks. A P1 deflection occurs at ~35 ms and is 1-4 times the magnitude of the N1. An N2 rebound occurs at ~50 ms at a magnitude that varies across studies. Finally, a P2 deflection occurs at ~80 ms and is followed by a subsequent rise in amplitude and broader peak activity (not labeled). Note that in the TE response example (Figure 4a green), the magnitudes of the early peaks (i.e., TE N1 and P1) are comparable to each other yet smaller than the P2 deflection.

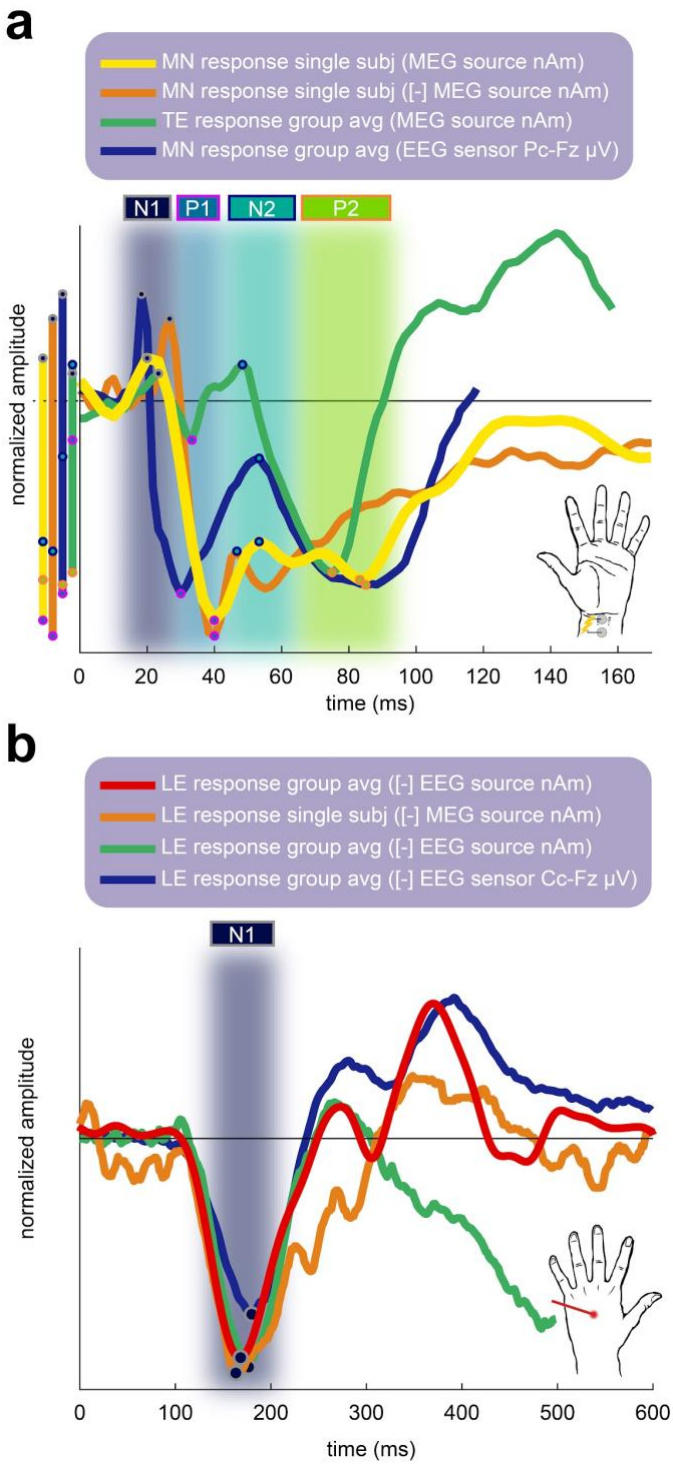

Figure 4. Primary deflections of the MN and LE responses are robust, reproducible, and conserved across multiple M/EEG experiments. The timing of the major deflections of the MN (a) and LE (b) responses are also common between sensor and source-space waveforms. (a) The representative MN response waveform analyzed in this study (yellow) is plotted alongside the following waveforms from prior studies with the N1 deflection pointed upward: orange, reproduced from (Lin et al., 2003); green, reproduced from (Jones et al., 2007); and blue, computed as the average potential from the contralateral parietal electrodes (Pc: P3 or P4) referenced to Fz in the dataset from (Lenoir et al., 2017). Normalized peak deflection amplitudes are plotted for each respective waveform on vertical bars in the left margin. (b) The representative LE response waveform analyzed in this study (red) is plotted alongside the following waveforms from prior studies with the N1 deflection pointed downward: orange, reproduced from (Raij et al., 2003); green, reproduced from (Schlereth et al., 2003); and blue, computed as the average potential

from the contralateral central electrodes (Cc: C3 or C4) referenced to Fz in the dataset from (Lenoir et al., 2017). [-] indicates that the sign of a given waveform has been reversed to reflect its underlying dipole direction in laminar neocortical source-space.

The primary conserved feature of the SI LE response waveforms in Figure 4b across studies and recording modalities is a large LE N1 deflection at ~170 ms followed by at least one rebound peak.

3.2. The MN response can be simulated from a sequence of SI activation similar to the sequence that generates a tactile evoked response, but with an additional early distal drive

We next applied HNN, which is designed to be a hypothesis development and testing tool, to interpret the cellular and circuit mechanisms contributing to the MN response. We focused on an example subject (Figures 1, 3, and 4, yellow), with the goal of interpreting the fundamentally conserved features of the MN response in Figure 4a. As described in the Methods, simulation experiments begin by defining a pattern of exogenous proximal and distal drives that activate the local network and drive current flow up and down the pyramidal neuron apical dendrites, creating positive and negative peaks, respectively, in the current dipole signal. Upward current flow is induced by excitatory synaptic depolarization of the proximal dendrites that drives passive current up apical dendrites and/or generates somatic action potentials that back-propagate up apical dendrites (see Figure 5d i). Conversely, downward current flow is induced by distal excitatory synaptic depolarization and/or somatic hyperpolarization that push and pull current down the apical dendrites, respectively (see Figure 5d ii). Figure 5a-c details these mechanisms in the context of a series of progressive simulations that lead to replication and detailed circuit interpretation of the MN responses.

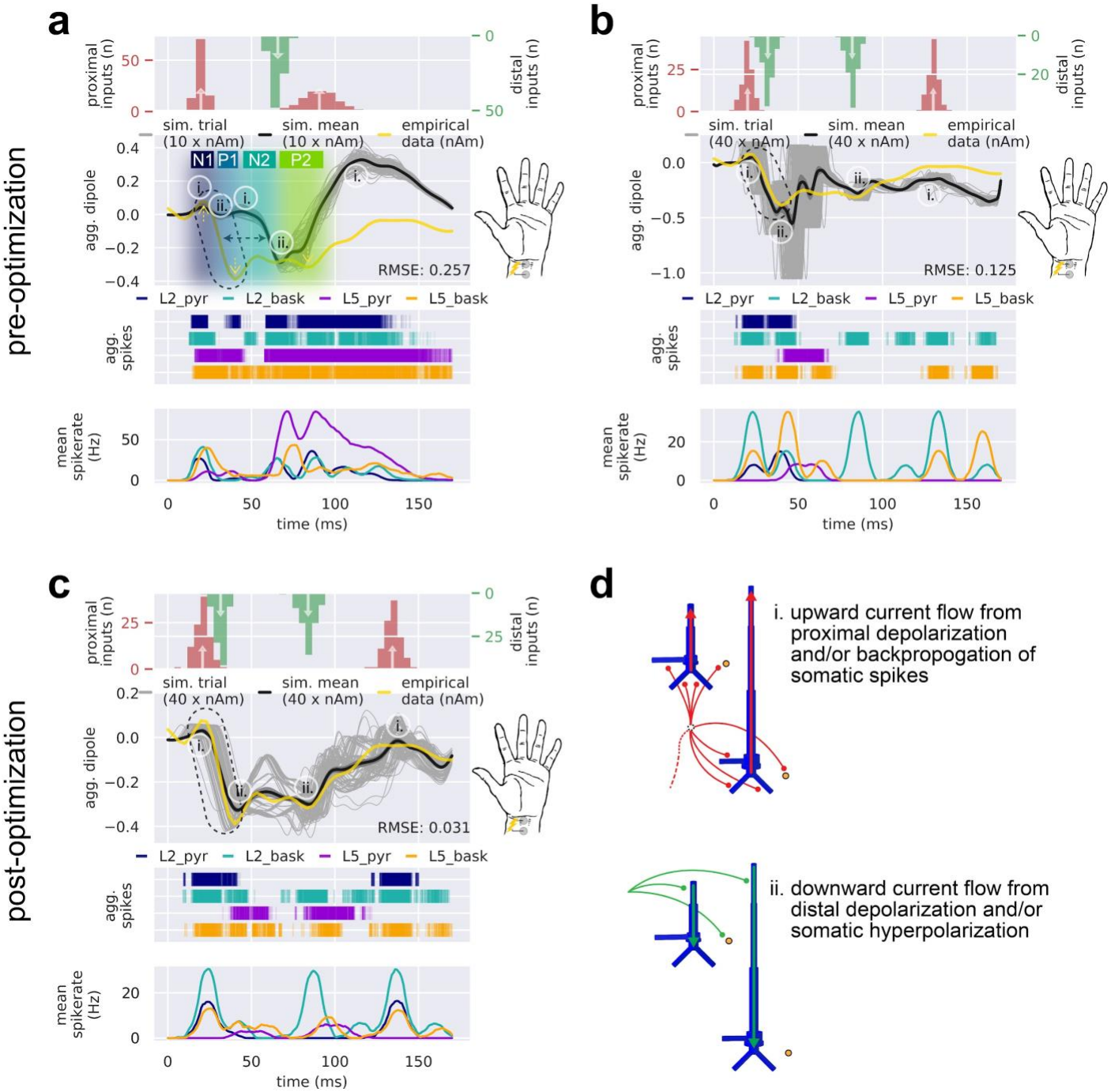

Figure 5. Simulating the MN response requires a sequence of four drives that begins with an initial proximal drive immediately followed by a strong distal drive. From top to bottom, panels (a-c) each contain the input drive histogram across all 100 trials (proximal, red; distal, green), aggregate simulated dipole (individual trials, grey traces n=100; trial-mean, black trace) alongside the empirical MN response (yellow trace), aggregate spike raster for all neurons over all trials according to type (L2 pyramidal, navy; L2 basket, cyan; L5 pyramidal, violet; L5 basket, orange), and population-mean spikerate (i.e., the average spikerate of a neuron of a given type). (a) The suprathreshold TE response as simulated in (Neymotin et al., 2020) produces a prominent negative deflection at t≅65 ms; however, it fails to produce the earliest MN P1 deflection (dotted line). Note that the TE response simulation uses non-synchronous driving inputs (i.e., drive spikes that are distributed across both time and cells for a given trial). (b) With the addition of a manually-tuned distal drive at t≅30 ms, we simulate the early upward-downward dynamic responsible for the MN N1 and P1 observed in the empirical data. (c) Upon parameter optimization of the drive sequence in (b), all deflections and temporal features of the empirical MN response are present in the simulated response. (d) Circuit mechanisms

responsible for upward and downward current flow in the HNN model. Simulated current dipole trials in (a and c) are smoothed by convolution with a 5 ms-wide Hamming window and dipole trials in (b) are smoothed by convolution with a 20 ms Hamming window.

Using the similarities between the temporal profiles of the empirical MN and suprathreshold TE responses (Figure 4a, yellow and green), we began our investigation by examining if the same sequence of exogenous drive used to model the TE response in prior studies (Neymotin et al., 2020) could re-create the MN response in the local SI network used here. This sequence is shown in the histograms at the top of Figure 5a and consists of a proximal drive at t≅20 ms, distal drive at t≅65 ms, and a re-emergent proximal drive at t≅90 ms. The simulated TE response contains five primary deflections labeled with i or ii corresponding to the underlying mechanisms of generation (Figure 5d). Proximal drive at t≅20 ms creates synaptic events that lead to depolarization and somatic spiking in the L2/3 and L5 pyramidal neurons (see spike histograms for each cell class across all 100 trials in Figure 5a, and layer specific responses in Supplementary Figure 1). The somatic action potentials generate strong and fast back-propagation of current up the apical dendrite creating a net upward current flow that accounts for the first positive peak (N1). The subsequent small negative deflection (P1) emerges from slightly delayed activation of the interneurons that inhibit the somas of the pyramidal neurons and pull current flow down the apical dendrites. The second positive peak (N2) reflects continued activation of the L5 pyramidal neuron near 40 ms. At t≅65 ms, a distal drive targets the distal apical dendrite of the L2/3 and L5 pyramidal neurons directly and causes current to flow downward towards the soma (top of Figure 5a, green histogram). Additionally, subsequent spiking of inhibitory cells induces hyperpolarizing currents at the pyramidal soma, pulling current downward toward the soma (see bottom panels of Figure 5a and Supplementary Figure 1a). The combination of these two effects accounts for the prominent negative deflection (P2) at t≅70 ms. The distal drive also generates subsequent spiking in the L2/3 and L5 pyramidal neurons, which together with the re-emergent proximal input at t≅90 ms induces current flow back up the apical dendrites to create the final positive deflection near 100 ms. Due to the longer length of the L5 pyramidal neurons, the net current dipole response is dominated by the activity in L5 (Supplementary Figure 1a).

With this pattern of activation, the simulated and empirical responses in Figure 5a are similar with some clear differences. Both have an initial positive N1 deflection (~20 ms), however, the TE simulation (solid black trace) lacks the prominent negative P1 deflection (~30 ms) and has a larger positive N2 peak (i.e., that rises above baseline; ~40 ms) compared to the MN response (yellow). Note in particular that the downward slope of the simulated TE response between the N2 and P2 deflections is also consistent with the slope between the empirical MN N1 and P1 (black dashed ellipse).

Given that the distal drive at ~65 ms was sufficient to create a negative P2 peak but the earlier prominent P1 peak at ~30 ms was missing (Figure 5a, dashed ellipse), we considered the effect of adding an

additional earlier distal drive at ~30 ms that could push current flow down the pyramidal neuron dendrites (Figure 5b). Together with the ~20 ms proximal drive, adding a distal drive at ~30 ms and manually tuning the timing and synaptic weight parameters created an upward-downward dynamic at ~20-40 ms that matched the MN N1 and P1 deflections (Figure 5b, black dashed ellipse; see Figure 6a,b for parameters corresponding to the TE and MN response simulations, respectively). Somatic inhibition also contributed to the prominent P1 generation, where prolonged activation of inhibitory cells in both L2/3 and L5 from 40-50 ms continued to pull current flow down the dendrites and the average current dipole remained negative (see also Supplementary Figure 1b). Some L5 pyramidal neurons were excited enough to spike, and their action potentials induced current flow up the dendrites, creating a slight positive rebound at ~60-70 ms but never reaching baseline. The remainder of the simulated MN response was generated by subsequent distal followed by a proximal drive which created the P2 and final rebound with similar mechanisms to those described for the TE response. The input times and strengths of these later inputs were adjusted slightly from Figure 5a via hand tuning, creating a different pattern of underlying spiking activity dominated by inhibitory spiking (distal: ~80 ms, proximal: 135 ms). Parameter optimization over these pre-OPS parameters rendered a mean aggregate dipole with improved fit to the empirical data and resurgence of pyramidal neuron spiking in the later portions of the response (Figure 5c, RMSE 0.031 compared to pre-OPS 0.125; all parameter values in Figure 6).

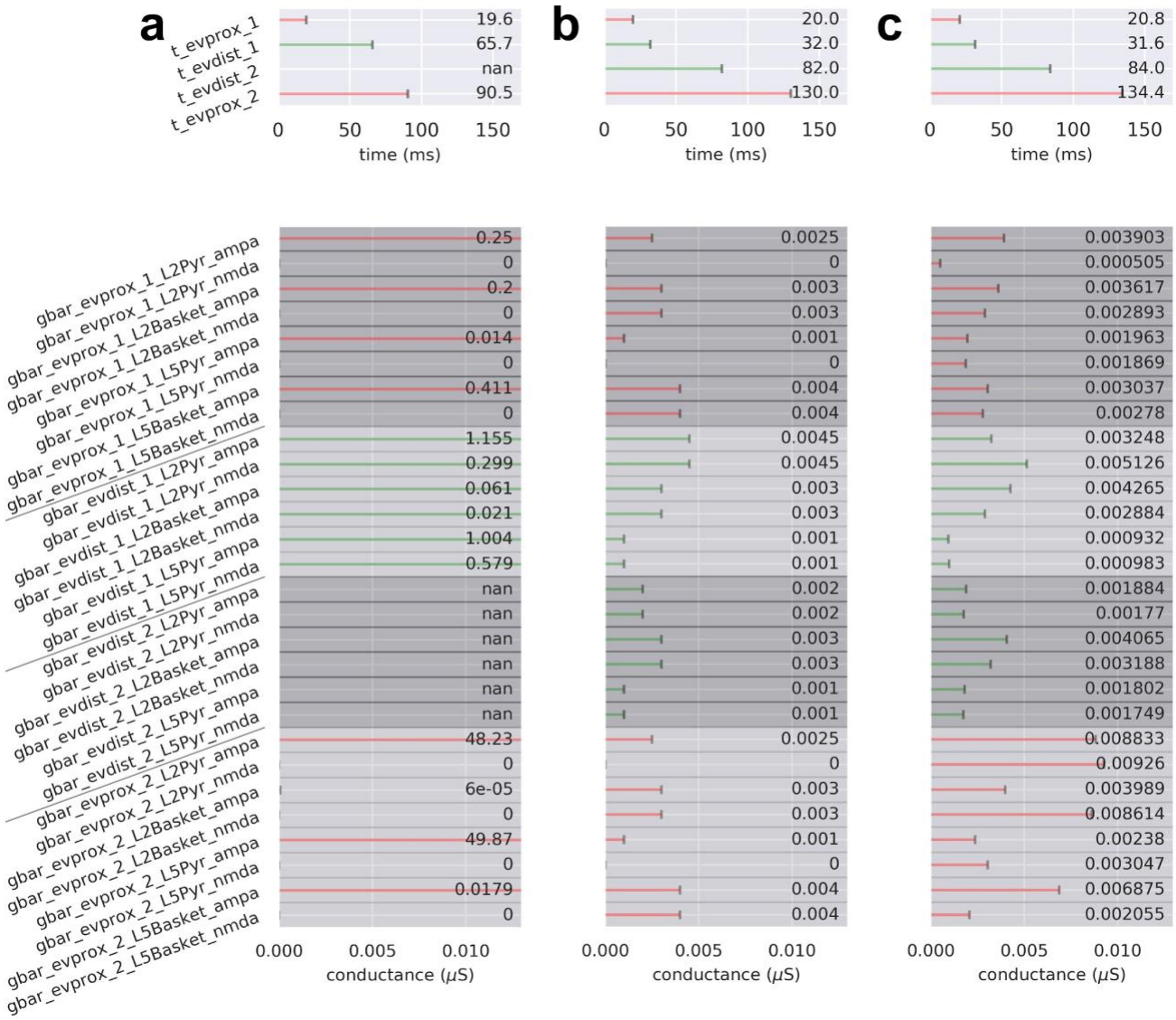

Figure 6. Drive parameters for the MN response simulations shown in Figure 5. For panels (a-c), there are four possible sequential drives: an early proximal drive (evprox_1), a subsequent distal drive (evdist_1), a late distal drive (evdist_2), and late evoked proximal drive (evprox_2). Each drive has a mean spike time (prefix 't'; top) and synaptic weights (prefix 'gbar'; bottom) associated with the drive's connectivity and available neurotransmitter receptors. Parameter values denoted by 'not a number' (nan) correspond to an omitted drive. (a) Simulation with three drives evprox_1, evdist_1, and evprox_2 at times t=19.6±2.5 (mean±SD), 65.7±3.8, and 90.5±10.4 ms, respectively. (b) Simulation with all four possible drives: a proximal, 2 distal, and a proximal at times t=20.0±3.0, 32.0±3.0, 82.0±3.0, and 130.0±3.0 ms, respectively. (c) Same as in (b) except at times t=20.8±4.1, 31.6±2.7, 84.0±4.5, and 134.4±4.4 ms, respectively.

In summary, while the timing and synaptic weights of the simulated MN response drives differed from those of the TE response, the basic sequence of events remained similar with the important exception that the MN response required an additional distal drive at t≅30 ms in order to produce the strong negative P1 deflection.

3.3. The LE N1 can be generated by a burst of repetitive distal drives that induces prolonged inhibitory activation

The LE response differs from the MN response in several ways (e.g., Figure 1). In contrast to the first MN deflection (MN N1) that occurs at ~25ms, lasts only ~20 ms, and is oriented upward, the first deflection of the LE response occurs at ~170 ms (LE N1), lasts ~150ms, and is oriented downward. The downward orientation of the LE N1 corresponds to current flow travelling from superficial to deep layers of the cortex. As such, we applied HNN to investigate perturbations to the local SI circuit that create downward currents, are slow to arrive to SI, and last for an extended period of time (i.e., >100 ms). We hypothesized that the long lasting effects could occur either through a single short duration driving input with a long-duration response, or through repetitive drives that cumulatively account for a long-duration response time through successive activation. As detailed below, exploration of these alternative hypotheses suggests that a burst of four repetitive distal drives with an inter-drive-interval (IDI) of 25 ms produces the prominent, prolonged downward deflection that best matched the empirical LE N1 deflection.

Recalling that the mechanisms that create downward deflections include excitatory distal drive, and/or activation of somatic inhibitory currents (Figure 5d), we first examined the possibility that the LE N1 is created by a single short duration distal drive (Figure 7a) or a burst of repetitive distal drives (Figure 7b).

Figure 7a shows the model's response to a single short duration distal drive at t=120±8.0 ms. Here, the post-synaptic conductances were manually tuned to get an approximate fit to the LE NI (parameters shown in Figure 8a). Initial excitation at the distal portion of the pyramidal apical dendrite pushes current down towards the soma. Additional activation of L2/3 and L5 inhibitory cells produces large and sustained downward current flow via both fast and slow somatic hyperpolarization. Note that the delayed L5 inhibitory neuron activity is induced via the excitatory connection from the L2/3 pyramidal neuron to L5 inhibitory neuron; see Figure 2 and Table 1. The majority of the sustained downward aggregate current dipole is produced by the L5 pyramidal cells, due at least in part to the length of their long apical dendrites and slow inhibition from L5 inhibitory cells (Supplementary Figure 2a).

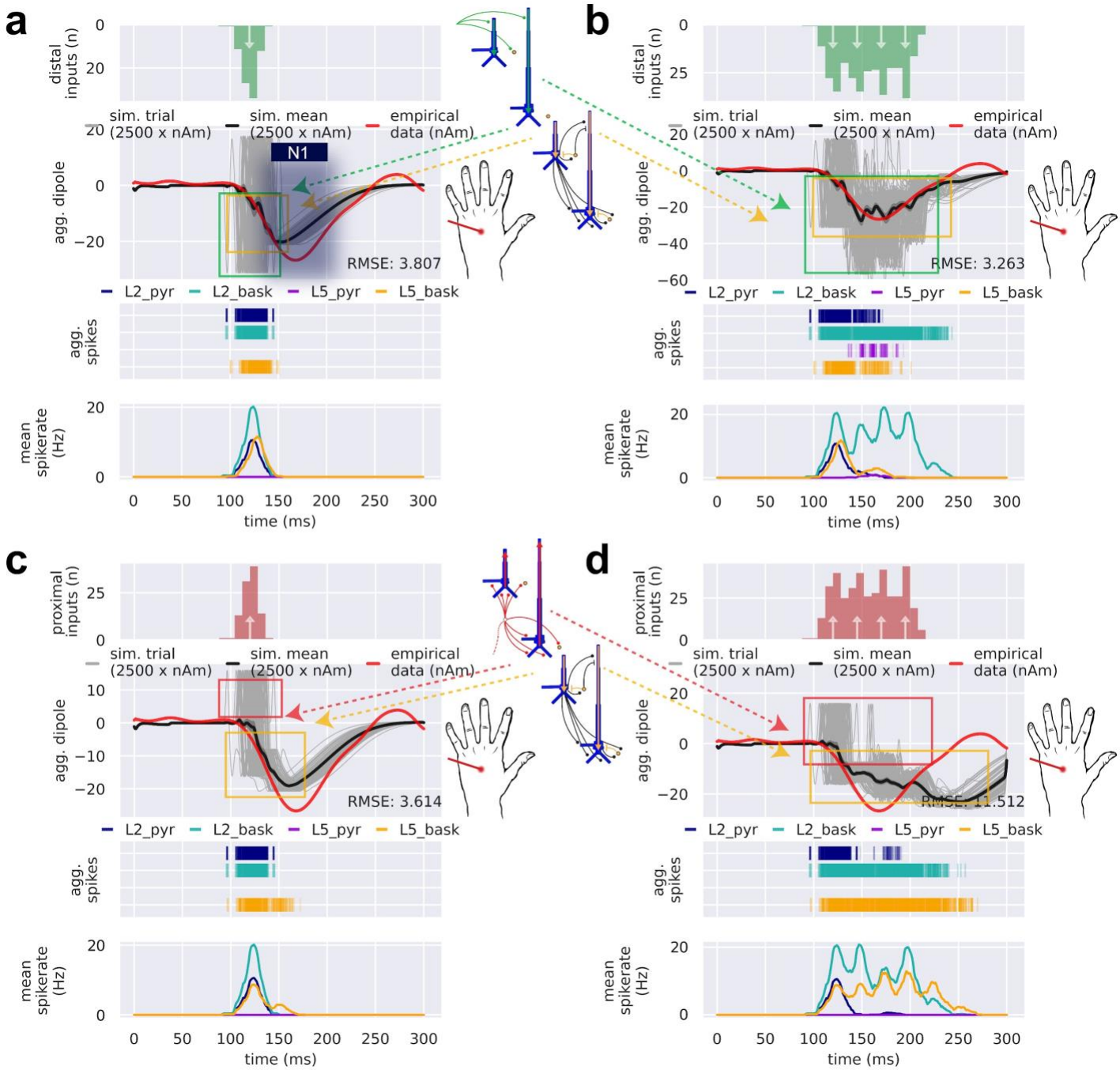

Figure 7. Prolonged downward current flow of the LE N1 requires strong activation of inhibitory cells. Multiple drive configurations can be employed to accomplish inhibitory basket cell activation, yet repetitive distal drives evoke a current dipole that best matches the depth and breadth of the empirical LE N1. From top to bottom, panels (a-d) each contain the input drive histogram across all 100 trials (proximal, red; distal, green), aggregate simulated dipole (individual trials, grey traces n=100; trial-mean, black trace) alongside the empirical LE response (red trace), aggregate spike raster for all neurons over all trials according to type (L2 pyramidal, navy; L2 basket, cyan; L5 pyramidal, violet; L5 basket, orange), and population-mean spikerate (i.e., the average spikerate of a neuron of a given type). (a) A single distal drive at t=120 ms results in a negative mean aggregate current dipole that lasts about 125 ms beginning at the onset of the LE N1. Initial excitation at the distal apical dendrite of a pyramidal cell drives current down the dendrite towards the soma. The subsequent sustained downward deflection in each simulation trial results from inhibition at the soma drawing current down the apical dendrite for a prolonged period of time. (b) A burst of four repetitive distal drives starting at t=120 ms and ending at t=195 ms creates a larger and more prolonged mean aggregate dipole deflection compared to the simulation in (a). (c) A single proximal drive can produce a mean aggregate current dipole similar to that of a

single distal drive, except through initial excitatory input that targets pyramidal and basket cell somas. As in (a), subsequent activation of basket cells creates strong inhibition that results in a dominant somatic hyperpolarizing current. (d) A burst of four repetitive proximal drives with the same temporal profile as in (b) creates a mean aggregate dipole that extends well past 250 ms. Simulated current dipole trials in (a-d) are smoothed by convolution with a 5 ms-wide Hamming window.

While a single short duration distal drive produced a close fit to the empirical LE N1 deflection, the response did not reach the full depth and breadth of the deflection. Optimization of the distal drive parameters did not improve the fit and the deflection instead plateaued, still failing to match the depth and breadth of the empirical LE N1 (Supplementary Figure 3a).

We next examined if a burst of repetitive distal drives could induce an LE N1 deflection that more closely matches the depth and breadth of the empirical data. Through exploration of different burst patterns (data not shown), we found that repetitive distal drives applied at regular intervals of ~25ms over the course of the N1 deflection produced the best match. Figure 7b shows that repetitive distal drives comprised of inputs at t=120.0±8.0 (mean±SD), 145.0±8.0, 170.0±8.0, and 195.0±8.0 ms create a deeper and more prolonged mean aggregate dipole deflection, closer to the empirical LE N1 (parameters shown in Figure 8b). Similar to the single distal drive, the first drive of the burst delivers distal depolarization of the pyramidal neurons followed by somatic hyperpolarization that together produce a downward current dipole in the pyramidal cells, with the early response dominated by activity in L5 (Supplementary Figure 2b). With each successive distal drive, inhibitory neurons in L2/3 are re-activated creating prolonged and cumulative somatic hyperpolarization of the L2/3 pyramidal neurons that dominates the later portion of the response (see spike raster and aggregate spikerate in Figure 7b, bottom panels, and Supplementary Figure 2b).

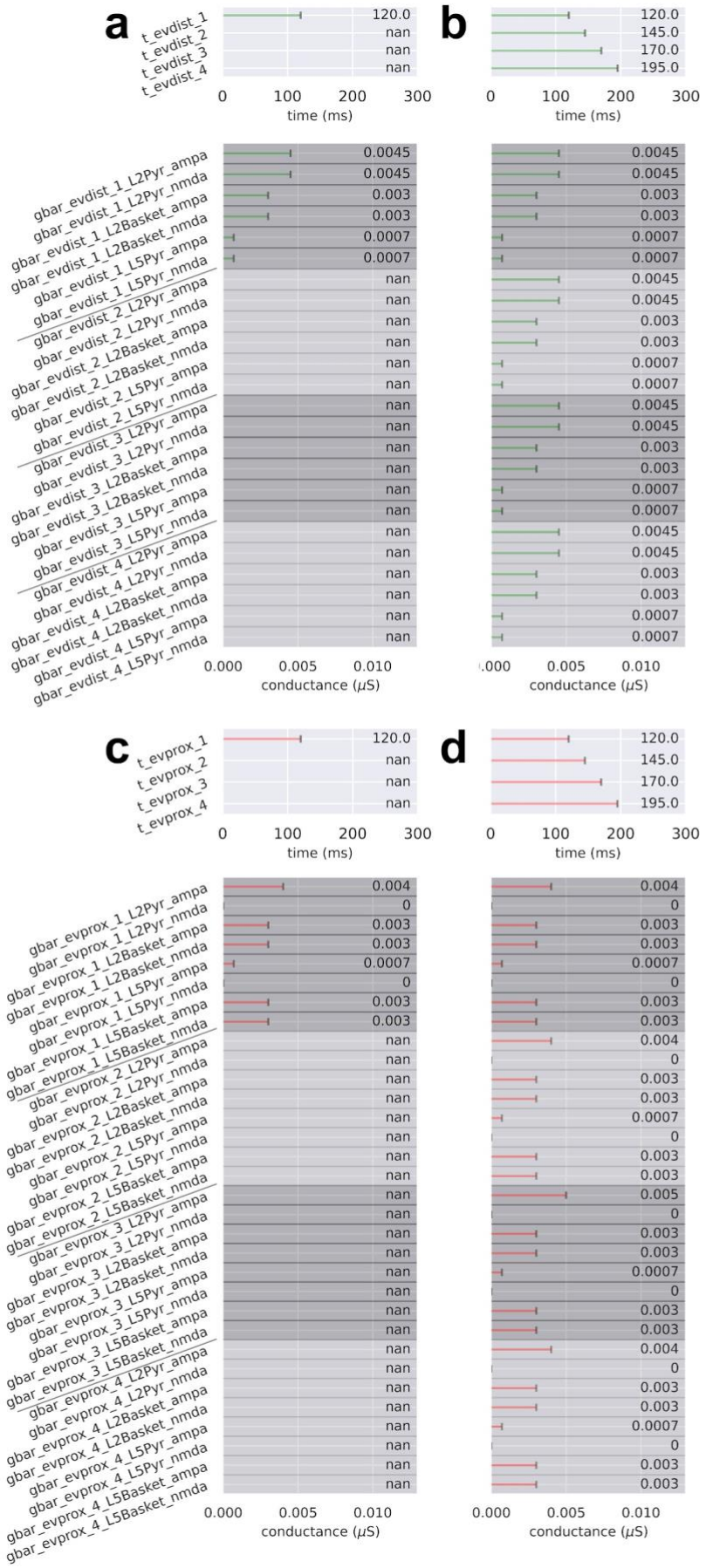
a
t_evdist_1
t_evdist_2
t_evdist_3
t_evdist_4
120.0
nan
nan
nan
0
100
200
300
time (ms)
b
120.0
145.0
170.0
195.0
time (ms)
gbar_evdist_1_L2Pyr_ampa
gbar_evdist_1_L2Pyr_nmda
gbar_evdist_1_L2Basket_ampa
gbar_evdist_1_L2Basket_nmda
gbar_evdist_1_L5Pyr_ampa
gbar_evdist_1_L5Pyr_nmda
gbar_evdist_2_L2Pyr_ampa
gbar_evdist_2_L2Pyr_nmda
gbar_evdist_2_L2Basket_ampa
gbar_evdist_2_L2Basket_nmda
gbar_evdist_2_L5Pyr_ampa
gbar_evdist_2_L5Pyr_nmda
gbar_evdist_3_L2Pyr_ampa
gbar_evdist_3_L2Pyr_nmda
gbar_evdist_3_L2Basket_ampa
gbar_evdist_3_L2Basket_nmda
gbar_evdist_3_L5Pyr_ampa
gbar_evdist_3_L5Pyr_nmda
gbar_evdist_4_L2Pyr_ampa
gbar_evdist_4_L2Pyr_nmda
gbar_evdist_4_L2Basket_ampa
gbar_evdist_4_L2Basket_nmda
gbar_evdist_4_L5Pyr_ampa
gbar_evdist_4_L5Pyr_nmda
0.0045
0.003
0.0007
0.000
0.005
0.010
conductance (μS)
c
t_evprox_1
t_evprox_2
t_evprox_3
t_evprox_4
d
gbar_evprox_1_L2Pyr_ampa
gbar_evprox_1_L2Pyr_nmda
gbar_evprox_1_L2Basket_ampa
gbar_evprox_1_L2Basket_nmda
gbar_evprox_1_L5Pyr_ampa
gbar_evprox_1_L5Pyr_nmda
gbar_evprox_1_L5Basket_ampa
gbar_evprox_1_L5Basket_nmda
gbar_evprox_2_L2Pyr_ampa
gbar_evprox_2_L2Pyr_nmda
gbar_evprox_2_L2Basket_ampa
gbar_evprox_2_L2Basket_nmda
gbar_evprox_2_L5Pyr_ampa
gbar_evprox_2_L5Pyr_nmda
gbar_evprox_2_L5Basket_ampa
gbar_evprox_2_L5Basket_nmda
gbar_evprox_3_L2Pyr_ampa
gbar_evprox_3_L2Pyr_nmda
gbar_evprox_3_L2Basket_ampa
gbar_evprox_3_L2Basket_nmda
gbar_evprox_3_L5Pyr_ampa
gbar_evprox_3_L5Pyr_nmda
gbar_evprox_3_L5Basket_ampa
gbar_evprox_3_L5Basket_nmda
gbar_evprox_4_L2Pyr_ampa
gbar_evprox_4_L2Pyr_nmda
gbar_evprox_4_L2Basket_ampa
gbar_evprox_4_L2Basket_nmda
gbar_evprox_4_L5Pyr_ampa
gbar_evprox_4_L5Pyr_nmda
gbar_evprox_4_L5Basket_ampa
gbar_evprox_4_L5Basket_nmda
0.004
0
0.003
0.0007
0.005

572

Figure 8. Drive parameters for the LE response simulations shown in Figure 7. For panels (a-d), there are either one or four drives per simulation. Each drive has a mean spike time (prefix 't'; top) and synaptic weights (prefix 'gbar'; bottom) associated with the drive's connectivity and available neurotransmitter receptors. Parameter values denoted by 'not a number' (nan) correspond to an omitted drive. (a) Simulation with one distal drive (evdist_1) at time t=120.0±8.0 ms (mean±SD). (b) Simulation with four distal drives (evdist_1-evdist_4) at times t=120.0±8.0, 145.0±8.0, 170.0±8.0, and 195.0±8.0 ms, respectively. (c,d) Same as in (a) and (b), respectively, except with proximal instead of distal drive (evprox_1-evprox_4).

The ~25 ms IDI of the distal drive that produced a good fit to the empirical dipole, as described above, is equivalent to ~40 Hz gamma frequency drive. Further investigation of spiking activity in the network suggests that this drive frequency produces an optimal balance of inhibition and excitation in the L2/3 network by engaging prolonged somatic inhibition and minimizing pyramidal neuron firing (Supplementary Figure 4), which would negate the somatic hyperpolarization and push current up the dendrites (Figure 5d). The spike raster in Figure 7b shows that the L2/3 inhibitory neurons, as a population, spike rhythmically at ~40 Hz. This gamma resonance is due to strong inhibitory-to-inhibitory $GABA_A$ergic connections (Table 1) that have a ~25 ms time constant of decay, coupled with the gamma frequency distal drive to the inhibitory neurons. Gamma resonance due to fast reciprocal inhibition is an established mechanism known as Interneuron-Gamma (ING) (Tiesinga and Sejnowski, 2009; Wang and Buzsáki, 1996). This prolonged L2/3 inhibition suppresses pyramidal neuron firing in both L2/3 and L5, enabling the somatic hyperpolarization to produce a negative current dipole response. Supplementary Figure 4 shows that the ~25 ms IDI minimized pyramidal neuron firing more effectively than several other IDI configurations (and their associated frequencies) of the repetitive drive sequence.

The predominant mechanism creating the LE N1 deflection in Figure 7a,b is prolonged pyramidal neuron somatic inhibition mediated by a single or repetitive distal drive(s). However, an open question is if a strong proximal drive to the L2/3 and L5 inhibitory neurons, absent of a distal drive, might suffice to generate the N1. We tested this hypothesis by delivering a single proximal drive at t=120±8.0 ms (Figure 7c). This drive configuration produced a mean aggregate current dipole and spiking pattern similar to that of the single distal drive in Figure 7a. As with a single short duration distal input, the depth and breadth of the simulated N1 deflection did not match the empirical data. An attempt to manually deepen and prolong the N1 deflection with a burst of repetitive proximal drives, similar to the distal burst pattern in Figure 7b, did not improve fitting of the model to the experimental data and instead extended the response well past the end of the empirical LE N1 deflection (>250 ms; Figure 7d). Parameter optimization also did not adequately improve the fit from either the single or repetitive proximal drives (Figure 8c,d; Supplementary Figure 3c,d).

Concluding that a burst of repetitive distal drives with a 25 ms IDI provided the best fit to the LE N1 response, we next examined mechanisms that could account for subsequent rebound activity at ~250 ms (Figure 2b). Building from the simulations in Figure 7b, Figure 9a,b shows the LE response with an

additional late proximal drive at t=260±12.0 ms, before and after parameter optimization, respectively (Figure 10a,b). The late proximal drive can generate the positive deflecting rebound response through proximal depolarization and backpropagation of somatic spikes in the L2/3 and L5 pyramidal neurons, which together push current flow up the pyramidal neuron dendrites (post-optimization Figure 9b, middle and bottom plots). Parameter optimization preserved the temporal profile of the burst of distal drives (i.e., with a mean 25 ms IDI) and further decreased the RMSE.

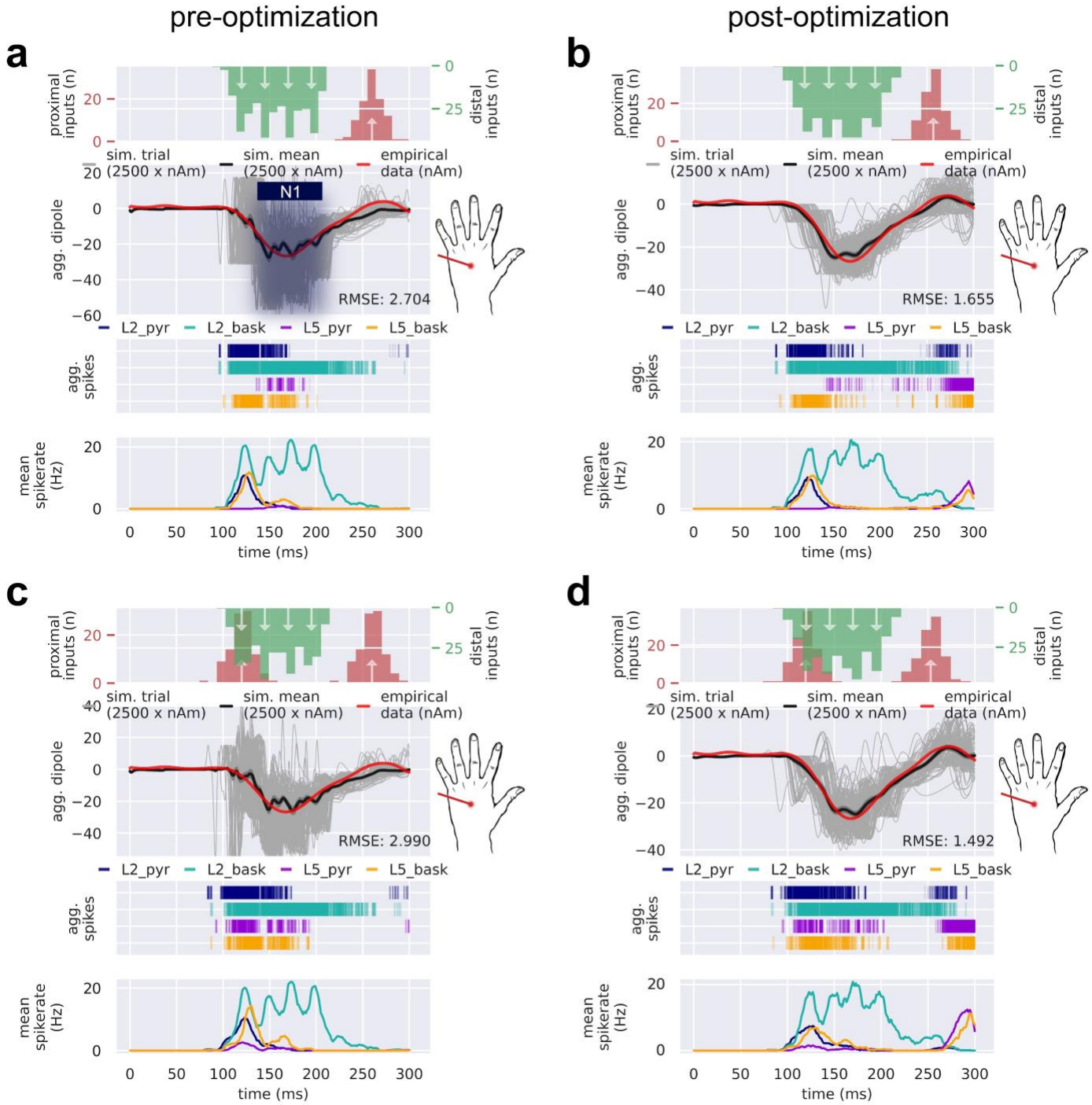

Figure 9. The LE N1 deflection along with its subsequent rebound can be simulated with a burst of repetitive distal drives, a late proximal drive, and an optional early proximal drive. From top to bottom, panels (a-d) each contain the input drive histogram across all 100 trials (proximal, red; distal, green), aggregate simulated dipole (individual trials, grey traces n=100;

trial-mean, black trace) alongside the empirical MN response (red trace), aggregate spike raster for all neurons over all trials according to type (L2 pyramidal, navy; L2 basket, cyan; L5 pyramidal, violet; L5 basket, orange), and population-mean spikerate (i.e., the average spikerate of a neuron of a given type). (a) A manually-tuned burst of repetitive distal drives with a late proximal drive at t=260 ms simulates the N1 deflection with its subsequent rebound. (b) Parameter optimization of the drive configuration shown in (a) conserves the temporal profile of driving inputs while improving the simulation fit to empirical data. (c) Same as in (a), except with an additional early proximal drive at t=120 ms. (d) (b) Parameter optimization of the drive configuration shown in (c) again conserves the temporal profile of driving inputs while further improving the simulation fit to empirical data. Simulated current dipole trials in (a,c) are smoothed by convolution with a 5 ms-wide Hamming window and trials in (b,d) are smoothed by convolution with a 20 ms Hamming window.

The sequence of distal (feedback) followed by proximal (feedforward) drive that generated the LE response in Figure 9b is remarkably different than the established cortical response to innocuous somatosensory stimulation, which begins with a feedforward drive via lemniscal thalamic input (e.g., MN N1 response in Figure 5). However, as a single proximal drive was able to replicate some features of the LE N1 response (Figure 7c) and the in vivo laminar profile of the LE response is unknown, we wanted to determine if a proximal-first sequence, similar to the MN drive sequence, could in fact produce the LE response. We tested this by adding an early proximal drive at t=120.0±12.0 ms (Figure 9c,d; Figure 10c,d) to the existing drive sequence for the LE response from Figure 9a,b. The net result of adding the early proximal input is an increase in early L5 pyramidal spiking at ~125 ms and a slightly improved fit to the empirical waveform post-optimization; however, the necessity of this early input is unknown. As addressed further in the Discussion, the model results here provide several targeted cortical features over which these alternative mechanisms can be tested further with invasive recordings or other imaging modalities

(e.g., early firing in the L5 pyramidal neurons would be consistent with an early proximal input).

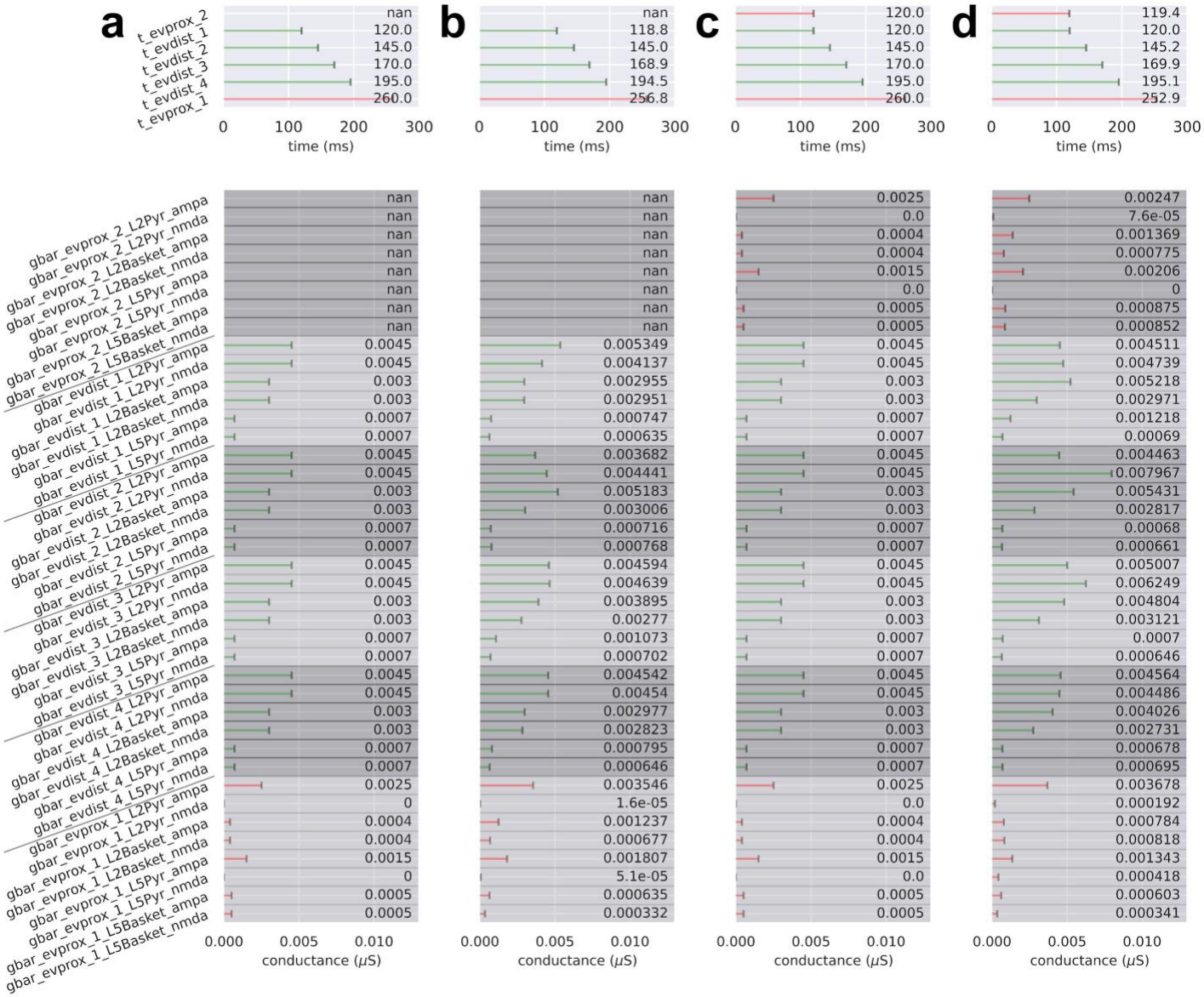

Figure 10. Drive parameters for the LE response simulations shown in Figure 9. For panels (a-d), there are six possible sequential drives: four distal drives (evdist_1-evdist_4), a proximal drive responsible for producing the rebound (evprox_1), and an optional early proximal drive (evprox_2). Each drive has a mean spike time (prefix 't'; top) and synaptic weights (prefix 'gbar'; bottom) associated with the drive's connectivity and available neurotransmitter receptors. Parameter values denoted by 'not a number' (nan) correspond to an omitted drive. (a) Simulation with distal drives evdist_1-evprox_4 and evprox_1 at times t=120.0±8.0 (mean±SD), 145.0±8.0, 170.0±8.0, 195.0±8.0, and 260.0±12.0 ms, respectively. (b) Same drive sequence as in (a) except at times t=118.8±10.0, 145.0±10.0, 168.9±9.2, 194.5±11.5, and 256.8±12.2 ms, respectively. (c) Same drive sequence as in (a) except with an early proximal drive, exprox_2, at t=120.0±12.0 ms. (d) Same drive sequence as in (c) except at times t=119.4±12.0, 120.0±10.0, 145.2±10.0, 169.9±8.8, 195.1±10.1 and 252.9±12.3 ms, respectively.

3.4. The simulated LE response exhibits robust gamma activity during the N1 deflection

Recent studies have shown that noxious laser stimulation produces a robust ~40 Hz gamma response in EEG sensors above SI along with an ~80 Hz high gamma response in humans (Heid et al., 2020), the latter of which was confirmed with electrocorticography (ECoG) and intracortical microelectrode recordings

in rodents (Hu and Iannetti, 2019; Yue et al., 2020). Given that inhibitory cell firing at ~40 Hz helps create the negative LE N1 deflection in the model simulations (Figure 7b and 9b,d, Supplementary Figure 4), we examined if the frequency response of the unsmoothed simulation near the LE N1 deflection exhibits 40 Hz activity, thus providing a potential circuit explanation for the prior empirical studies. Indeed, prominent ~40 Hz spectral activity was present in single-trial TFRs (Figure 11a-c) and the trial mean TFR (n=100 trials; Figure 11d) of the simulated LE response in Figure 9d, along with peaks at ≤5 Hz (theta-band) and ~80 Hz (high gamma-band). The 80 Hz activity emerges from the time course of the sharp deflections in the waveform that each last at most ~12.5 ms. The 40 Hz activity reflects the periodic nature of the downward dipole deflections occurring at ~25 ms intervals from somatic inhibition, as described above, and the ≤5 Hz activity comes from the slow downward component of the LE N1 deflection that lasts ~100 ms. These results are consistent across the simulations with and without an early proximal drive as presented in Figure 9b,d (comparison not shown).

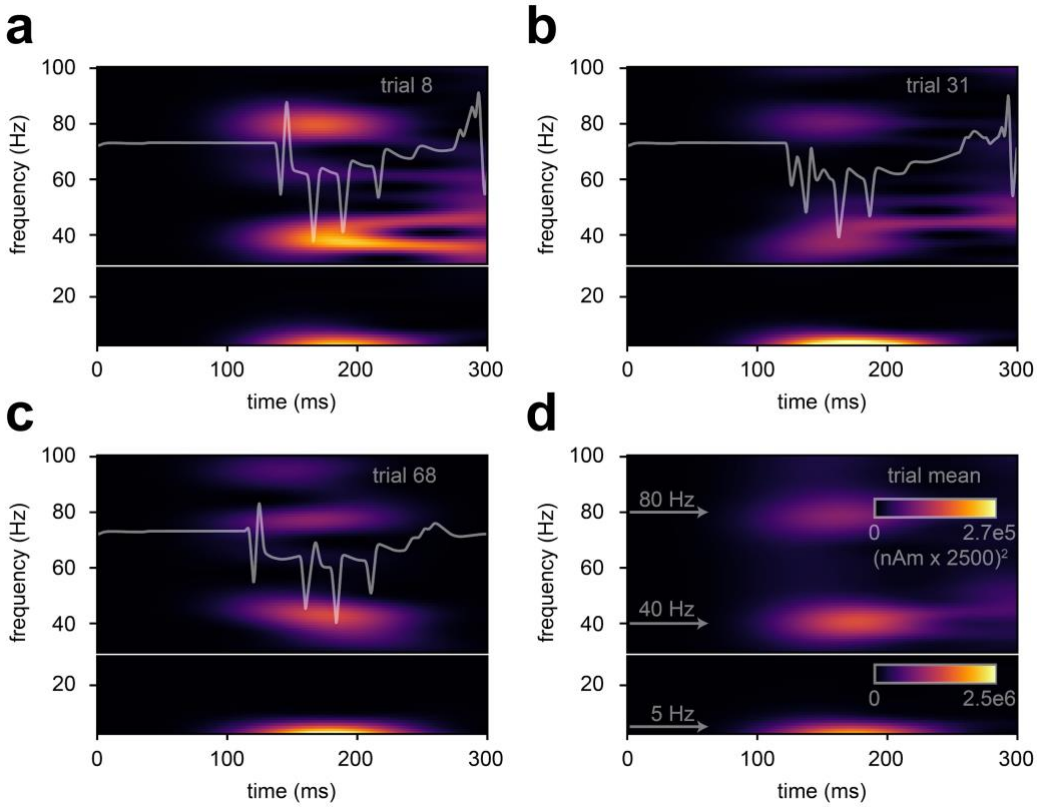

Figure 11. Repetitive distal drives in the optimized LE N1 simulation produce resonant spectral activity in the model SI circuit. (a-c) Time-frequency response (TFR) of three representative simulation trials. (d) Trial-mean TFR of individual simulation trials (n=100) reveals LE event related spectral activity at ~5, ~40, and ~80 Hz. Note that the TFR was calculated from simulation trials with minimal smoothing (i.e., by convolution with a 5 ms Hamming window) to preserve the high frequency components of each time course.

4. Discussion

M/EEG evoked responses from median nerve and laser stimulation are widely studied to gain insight into non-painful and painful somatosensory processing. The majority of prior studies describe how evoked

response features such as peak timing and amplitudes vary with stimulation conditions and/or perception. Here, we address the open question of the detailed neocortical circuit origin of the peaks in innocuous MN and noxious LE responses found in macroscale neural recordings. Analyzing data from prior published studies, we found that the peak timings and orientations of source localized responses in SI were conserved across studies and showed that each peak can be interpreted in terms of the corresponding current flow up and down pyramidal neuron apical dendrites (i.e., out of or into the cortex). We used a laminar model of the neocortex in the HNN simulation software to predict the detailed cell and circuit mechanisms underlying this current flow.

Building on prior studies of tactile evoked responses from a brief tap to the fingertip (Jones et al., 2009, 2007; Sliva et al., 2018; Ziegler et al., 2010), our modeling results predict that the mechanisms of the MN response are similar to those of the tactile evoked response and are generated from a sequence of layer specific feedforward (i.e., proximal), feedback (i.e., distal) and re-emergent feedforward drive to the local network, with the required addition of early distal drive at ~30 ms to generate the MN P1 (P30) peak. Unlike the MN response, the first peak in the LE response (N1) represents an inward current, which the model predicts emerges from an excitatory synaptic input to the supragranular layers (i.e., distal). Additionally, this distal input consists of repetitive drives at 40 Hz and produces gamma frequency activity in the model. Below, we place these predictions, as summarized in Figure 12, within the context of prior studies investigating the neural mechanisms of somatosensory processing and known anatomy and physiology of thalamocortical and cortico-cortical circuitry. We emphasize predicted signatures of circuit dynamics that can guide further testing with invasive recordings or other imaging modalities.

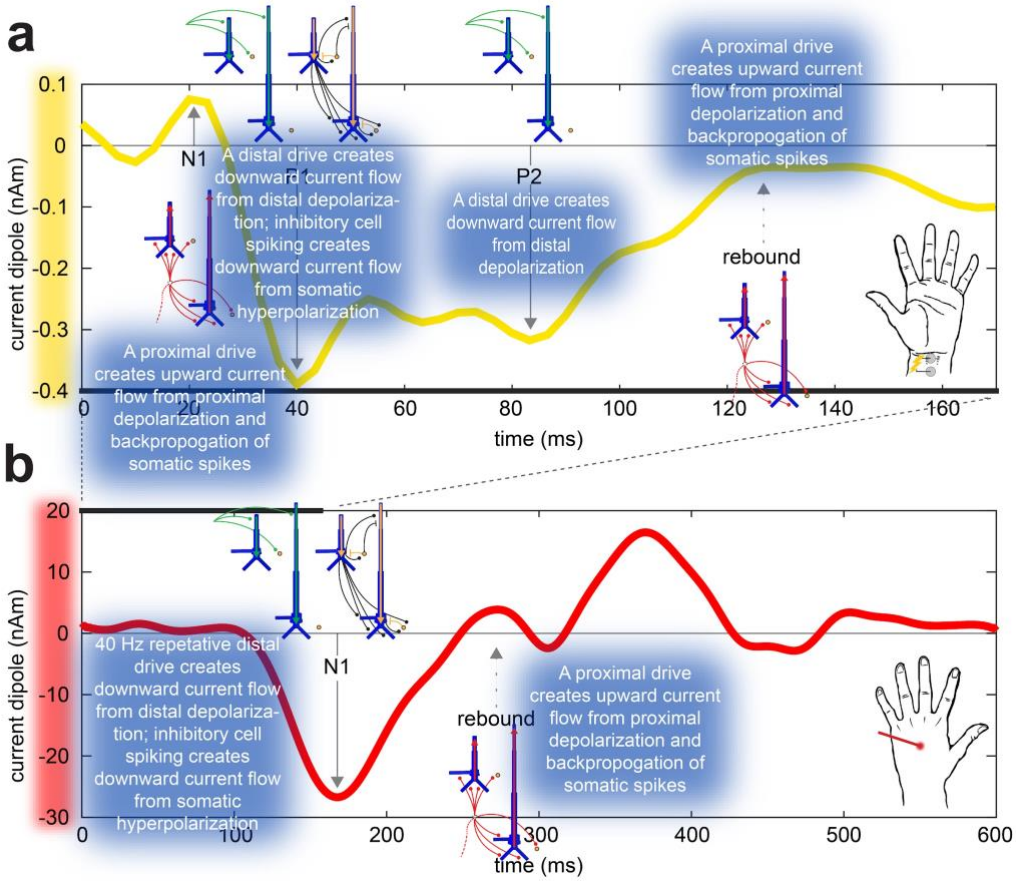

Figure 12. Summary of the predicted mechanisms that underlie each deflection of the respective MN and LE responses.

Overall, the HNN model's ability to produce both the MN and LE responses by only modulating the sequence of exogenous drives to the local network, with all local network parameters held constant (see Figure 2 and Table 1), supports the notion that the canonical features of a laminar neocortical network are capable of producing both innocuous and noxious responses. It should be noted that we make no claims about the relative number or overlap of the neuron populations responsible for generating the MN and LE responses within SI; rather we only posit that both evoked responses can emerge from canonical features of the SI network. We also make no specific claims about mechanisms underlying perception but focus on the mechanisms that produce features of the MN and LE responses, such as peak timings and orientations, that are conserved across studies. Our results lay the foundation for future investigations using median nerve and laser stimulation to study circuit mechanisms of non-painful and painful percepts and may help guide novel therapeutics for pathological somatosensation.

4.1. Model predictions extend prior understanding of the circuit mechanisms of the MN response

Consistent with previous studies, the modeling results here demonstrate that the first deflection of the MN response can be produced by feedforward excitatory synaptic drive to the granular layers of SI at ~20 ms. In the model, this input propagates directly to the proximal dendrites of pyramidal neurons in supra- and infragranular layers to induce current flow up the pyramidal apical dendrites (Cauller and Kulics, 1991;

Jones et al., 2007; Lipton et al., 2006; Peterson et al., 1995; Schroeder et al., 1995; Wikström et al., 1996). This drive likely originates in the ventrobasal thalamus (Cauller and Kulics, 1991; Jones et al., 1979; Yamada et al., 1984) as part of the lemniscal pathway that receives activation from fast Aβ fibers in the peripheral nerves (Burke et al., 1975).

Following the initial MN N1 (N20) deflection, our model predicts that an early distal drive at ~30 ms is necessary to produce the downward MN P1 (P30). This novel prediction deviates from an alternative notion in the literature that assumes the human M/EEG P1 deflection from median nerve (Wikström et al., 1996) and tactile stimulation (Jones et al., 2007), also known as the downward-pointing EEG/local field potential (LFP) N1 in rats (Bruyns-Haylett et al., 2017), originates from somatic hyperpolarization of pyramidal neurons via feedforward inhibition. While the precise pre-synaptic source of this predicted ~30 ms distal drive is unknown, likely candidates include the ventral medial thalamus or the secondary somatosensory cortex (SII) given that they both processes somatosensory signals and project into the superficial layers of SI (Cauller and Kulics, 1991; Friedman, 1983). Thus, we further predict that either the innocuous MN signal from the periphery branches somewhere in its ascending pathway, or there is a rapid thalamocortical loop of activity that creates both proximal and distal drive within the first ~30 ms post-stimulus.

In addition to creating the MN N1 and P1 deflections, the precise timing of the early proximal and distal drives relative to each other created an optimally excitable state that allowed backpropagation of pyramidal neuron spikes to generate the small upward-oriented N2 rebound before a subsequent distal drive at ~85 ms induced the prominent P2. In prior studies, the mechanistic origins of the MN N2 and P2 (historically referred to as N45 and P60) have been disputed over as emerging from either excitation followed by inhibition at the pyramidal soma (Gardner et al., 1984; Wikström et al., 1996), excitation at the pyramidal distal apical dendrite via a cortico-cortical projection that then causes current to passively flow down the dendrite toward the soma (Cauller and Kulics, 1991), or a combination of the two (Peterson et al., 1995). The model predictions are supportive of a combined mechanism, where local network spiking in the L5 pyramidal cells emerges from local excitatory synaptic interactions and creates the upward oriented N2 while simultaneous prolonged somatic inhibition keeps the N2 peak below zero. Finally, a late excitatory distal drive creates focal downward current flow during the P2.

The model results may also help explain the large amount of variability in the MN N2 response observed across studies (Figure 4a). Individual simulation trial responses show enhanced variability between 50-100 ms near the N2 peak (see grey traces in the second panel of Figure 5c). This variability comes from the stochastic nature of the arrival time of the initial proximal and distal drives before 50 ms (see red and green histograms in Figure 5c). This stochasticity produces varying amounts of GABAergic inhibitory tone onto the population of L5 pyramidal cells based on the elapsed time between the proximal and distal drive.

On trials with more inhibition, which is denoted by the brief suppression of population spiking across all cell types (Figure 5c), all L5 pyramidal neurons are suppressed and the N2 peak remains nearly flat, whereas on trials with less inhibition, L5 pyramidal neuron spiking creates backpropagating current and an upward N2 peak. The N2 peak, however, remains below zero because of the competing somatic inhibition. This prediction suggests that if MN stimulation is repeated at regular sub-second intervals, residual inhibition at t>150 ms will reduce the excitatory impact of the next stimulus' early proximal and distal drive. Such an impairment in excitation tips the balance of network spiking in favor of reduced pyramidal neuron spiking and GABA-mediated inhibition that would normally produce large N1 and P1 deflections while minimizing the N2 rebound. Consistent with the results of prior research that observed the impact of repetitive MN stimulation, this mechanism predicts MN N1 and P2 attenuation and MN N2 amplification with shortening of the inter-stimulus interval and may point toward the use of MN N1, P1, and N2 deflections as a proxy for GABAergic tone (Wikström et al., 1996). Furthermore, hysteresis of these deflections due to repetitive stimulation might contribute to a central representation for perceived sensory adaptation (Graczyk et al., 2018).

4.2 Model predicts that extrinsically-driven bursts of gamma oscillations combined with network resonance indicate nociceptive processing in SI

In contrast to the MN response, the first deflection of the LE response reflects an inward superficial-to-deep current which the model predicts emerges from excitatory drives to supragranular layers. These drives push current down the dendrites of the L2 pyramidal neurons and activate L2/3 and L5 soma-targeting inhibitory cells that simultaneously induce current flow down the pyramidal neuron dendrites. The exogenous source of these distal drives is currently unknown and is likely different from the ventrobasal lemniscal thalamic drive inducing the initial feedforward MN response. Not only does the LE response begin at a greater latency from stimulation onset (~170 ms), reflecting in part that it is transmitted through slow Aδ fibers from the periphery to the spinal cord (Bromm and Treede, 1984; Treede et al., 1995, 1988), but early LE supragranular drive likely hales from non-sensory-specific ventromedial thalamus (VM) (Borszcz, 2006; Desbois and Villanueva, 2001; Glenn et al., 1982; Monconduit et al., 2003, 1999) or from the secondary somatosensory cortex (SII) (Baumgärtner et al., 2006; Iannetti et al., 2005; Ploner et al., 1999; Qiu et al., 2006; Treede et al., 2003; Vierck et al., 2013). As such, the source of this initial drive may overlap with the exogenous source of drives that produce later MN deflections (Cauller and Kulics, 1991). While our model simulations predict that exogenous drive targeting the superficial layer is the primary mechanism through which the LE N1 deflection is generated, it remains unclear whether or not a feedforward input to the granular layer may also be present (Figure 9c,d). This early feedforward drive could originate from the ventral posterolateral nucleus (VPL) of the thalamus (Treede et al., 2003; Vierck et al., 2013). The simulation results produce distinguishing micro-circuit features that can help disambiguate the existence of this feedforward drive, such as early spiking activity in L5 pyramidal neurons (compare Figure 9b and 9d).

Additionally, the model predicts that a burst of repetitive distal drives spaced at ~25 ms intervals (i.e., low gamma period) produces the LE N1 deflection. Model simulations found that this burst of drives created non-phase-locked high (~80 Hz) and low (~40 Hz) gamma activity. This points toward a mechanistic link between the phase-locked LE N1 deflection and non-phase-locked gamma event-related synchronization (ERS) observed in prior studies (Heid et al., 2020). These results are also consistent with recent work that found significant spike-field coherence between single unit inhibitory neurons in the superficial layers of SI and nearby LFP/ECoG gamma-frequency ERS (Yue et al., 2020).

While our study does not make any claims about circuit mechanisms underlying perceived pain intensity with noxious LE stimulation, several of the predicted mechanisms can be related to prior pain studies. Numerous studies have observed that single-trial measurements of the SI LE response amplitude correlate with subjective pain ratings (Hu and Iannetti, 2019; Huang et al., 2013; Peng et al., 2018; Timmermann et al., 2001). However, our MN nerve results and other studies show that other forms of sensory stimuli (e.g., somatosensory, auditory, visual) can evoke similar waveforms features as the LE response, albeit in different brain regions (Mouraux and Iannetti, 2009) and that they grade with perceptual intensity (Hu and Iannetti, 2019). The implied conclusion has been that the LE response waveform lacks the ability to encode nociceptive-specific processing and that peaks of the LE response are rather indirect measures of nociceptive processing that are easily biased by saliency (Iannetti et al., 2008). Perhaps a more direct measure of pain intensity is the magnitude of induced gamma-band oscillations near the time of the LE N1. The magnitude of gamma-band ERS correlates with perceived noxious stimulus intensity (Peng et al., 2018), is independent of saliency (Zhang et al., 2012), and predicts nociceptive-specific perception both within and across subjects (Heid et al., 2020; Hu and Iannetti, 2019). Further evidence suggests that spontaneous bursts of EEG gamma-band activity emerging from EEG electrodes over SI can differentiate human participants who are experiencing chronic pain from those who are not (Levitt et al., 2020).

As mentioned above, our results provide a detailed interpretation of the circuit mechanisms creating the gamma ERS. This mechanism relies on the repeated ~40 Hz gamma-frequency activation of L2/3 inhibitory neurons. Remarkably, this prediction is consistent with the finding that 40 Hz optogenetic drive of parvalbumin-positive inhibitory interneurons (PV) in mice led to nociceptive hypersensitivity and aversive behavior to innocuous contextual cues (Tan et al., 2019). While this finding did not motivate the choice of gamma frequency drive demonstrated in the present study, the cohesion with many prior studies suggests interneuron mediated gamma oscillations are a marker of painful nociceptive processing (Tan et al., 2019; Yue et al., 2020).

5. Conclusions

This study applied the HNN neural modeling software to make multi-scale predictions about neural mechanisms producing human SI evoked responses to non-painful MN and painful LE stimuli. We tuned the timing and sequence of distal and proximal drives to the model SI network to replicate empirically derived MN and LE evoked responses. Using the underlying architecture of HNN, we identified potential cellular and circuit mechanisms that mediate these somatosensory evoked responses. Our modeling predictions complement prior research that detail the neural dynamics of sensory processing and provide several targets for further testing of novel circuit mechanisms with invasive electrophysiological recordings (e.g., multi-electrode array recordings or ECoG) or other imaging modalities (e.g., layer resolved MEG (Bonaiuto et al., 2021) or magnetic resonance spectroscopy). Ultimately, these findings may help with the development of new diagnostic methods and targeted therapeutics for pain and pathological somatosensation.

Acknowledgments

We thank Lauri Parkkonen for helpful discussion regarding the MEG MN response data which we conducted HNN analysis on. We also thank Cedric Lenoir and André Mouraux for providing EEG sensor-space MN and LE response data. HNN simulations were conducted using computational resources and services at the Center for Computation and Visualization, Brown University. This study was supported by the National Institute of Biomedical Imaging and Bioengineering, National Institute of General Medical Sciences, and National Institute of Neurological Disorders and Stroke of the National Institutes of Health under awards R01EB022889, P20GM103645, and R01NS108414, respectively. The content is solely the responsibility of the authors and does not necessarily represent the official views of the National Institutes of Health.

Declarations of Interests

None

References

Almeida, T.F., Roizenblatt, S., Tufik, S., 2004. Afferent pain pathways: a neuroanatomical review. Brain Res., Brain Research Volume 1000 1000, 40–56. https://doi.org/10.1016/j.brainres.2003.10.073

Baumgärtner, U., Tiede, W., Treede, R.-D., Craig, A.D. (Bud), 2006. Laser-Evoked Potentials Are Graded and Somatotopically Organized Anteroposteriorly in the Operculoinsular Cortex of Anesthetized Monkeys. J. Neurophysiol. 96, 2802–2808. https://doi.org/10.1152/jn.00512.2006

Baumgärtner, U., Vogel, H., Ohara, S., Treede, R.-D., Lenz, F., 2011. Dipole source analyses of laser evoked potentials obtained from subdural grid recordings from primary somatic sensory cortex. J. Neurophysiol. 106, 722–730. https://doi.org/10.1152/jn.00135.2011

Bonaiuto, J.J., Little, S., Neymotin, S.A., Jones, S.R., Barnes, G.R., Bestmann, S., 2021. Laminar dynamics of high amplitude beta bursts in human motor cortex. NeuroImage 242, 118479. https://doi.org/10.1016/j.neuroimage.2021.118479

Borszcz, G.S., 2006. Contribution of the ventromedial hypothalamus to generation of the affective

dimension of pain. Pain 123, 155–168. https://doi.org/10.1016/j.pain.2006.02.026
Bromm, B., Treede, R.D., 1984. Nerve fibre discharges, cerebral potentials and sensations induced by CO2 laser stimulation. Hum. Neurobiol. 3, 33–40.
Bruyns-Haylett, M., Luo, J., Kennerley, A.J., Harris, S., Boorman, L., Milne, E., Vautrelle, N., Hayashi, Y., Whalley, B.J., Jones, M., Berwick, J., Riera, J., Zheng, Y., 2017. The neurogenesis of P1 and N1: A concurrent EEG/LFP study. NeuroImage 146, 575–588. https://doi.org/10.1016/j.neuroimage.2016.09.034
Burke, D., Mackenzie, R.A., Skuse, N.F., Lethlean, A.K., 1975. Cutaneous afferent activity in median and radial nerve fascicles: a microelectrode study. J. Neurol. Neurosurg. Psychiatry 38, 855–864. https://doi.org/10.1136/jnnp.38.9.855
Cauller, L.J., Kulics, A.T., 1991. The neural basis of the behaviorally relevant N1 component of the somatosensory-evoked potential in SI cortex of awake monkeys: evidence that backward cortical projections signal conscious touch sensation. Exp. Brain Res. 84, 607–619. https://doi.org/10.1007/BF00230973
Christmann, C., Koeppe, C., Braus, D.F., Ruf, M., Flor, H., 2007. A simultaneous EEG–fMRI study of painful electric stimulation. NeuroImage 34, 1428–1437. https://doi.org/10.1016/j.neuroimage.2006.11.006
Deiber, M.P., Giard, M.H., Mauguiere, F., 1986. Separate generators with distinct orientations for N20 and P22 somatosensory evoked potentials to finger stimulation? Electroencephalogr. Clin. Neurophysiol. Potentials Sect. 65, 321–334. https://doi.org/10.1016/0168-5597(86)90012-2
Desbois, C., Villanueva, L., 2001. The organization of lateral ventromedial thalamic connections in the rat: a link for the distribution of nociceptive signals to widespread cortical regions. Neuroscience 102, 885–898. https://doi.org/10.1016/S0306-4522(00)00537-6
Friedman, D.P., 1983. Laminar patterns of termination of cortico-cortical afferents in the somatosensory system. Brain Res. 273, 147–151. https://doi.org/10.1016/0006-8993(83)91103-4
Gardner, E.P., Hämäläinen, H.A., Warren, S., Davis, J., Young, W., 1984. Somatosensory evoked potentials (SEPs) and cortical single unit responses elicited by mechanical tactile stimuli in awake monkeys. Electroencephalogr. Clin. Neurophysiol. 58, 537–552. https://doi.org/10.1016/0013-4694(84)90044-0
Glenn, L.L., Hada, J., Roy, J.P., Deschesˆnes, M., Steriade, M., 1982. Anterograde tracer and field potential analysis of the neocortical layer I projection from nucleus ventralis medialis of the thalamus in cat. Neuroscience 7, 1861–1877. https://doi.org/10.1016/0306-4522(82)90003-3
Graczyk, E.L., Delhaye, B.P., Schiefer, M.A., Bensmaia, S.J., Tyler, D.J., 2018. Sensory adaptation to electrical stimulation of the somatosensory nerves. J. Neural Eng. 15, 046002. https://doi.org/10.1088/1741-2552/aab790
Gramfort, A., Luessi, M., Larson, E., Engemann, D.A., Strohmeier, D., Brodbeck, C., Goj, R., Jas, M., Brooks, T., Parkkonen, L., Hämäläinen, M., 2013. MEG and EEG data analysis with MNE-Python. Front. Neurosci. 7. https://doi.org/10.3389/fnins.2013.00267
Gramfort, A., Luessi, M., Larson, E., Engemann, D.A., Strohmeier, D., Brodbeck, C., Parkkonen, L., Hämäläinen, M.S., 2014. MNE software for processing MEG and EEG data. NeuroImage 86, 446–460. https://doi.org/10.1016/j.neuroimage.2013.10.027
Hämäläinen, M., Hari, R., Ilmoniemi, R.J., Knuutila, J., Lounasmaa, O.V., 1993. Magnetoencephalography---theory, instrumentation, and applications to noninvasive studies of the working human brain. Rev. Mod. Phys. 65, 413–497. https://doi.org/10.1103/RevModPhys.65.413
Heid, C., Mouraux, A., Treede, R.-D., Schuh-Hofer, S., Rupp, A., Baumgärtner, U., 2020. Early gamma-oscillations as correlate of localized nociceptive processing in primary sensorimotor cortex. J. Neurophysiol. 123, 1711–1726. https://doi.org/10.1152/jn.00444.2019
Hu, L., Iannetti, G.D., 2019. Neural indicators of perceptual variability of pain across species. Proc. Natl. Acad. Sci. 116, 1782–1791. https://doi.org/10.1073/pnas.1812499116
Huang, G., Xiao, P., Hung, Y.S., Iannetti, G.D., Zhang, Z.G., Hu, L., 2013. A novel approach to predict subjective pain perception from single-trial laser-evoked potentials. NeuroImage 81, 283–293. https://doi.org/10.1016/j.neuroimage.2013.05.017
Huttunen, J., Komssi, S., Lauronen, L., 2006. Spatial dynamics of population activities at S1 after median and ulnar nerve stimulation revisited: An MEG study. NeuroImage 32, 1024–1031. https://doi.org/10.1016/j.neuroimage.2006.04.196

Iannetti, G.D., Hughes, N.P., Lee, M.C., Mouraux, A., 2008. Determinants of Laser-Evoked EEG Responses: Pain Perception or Stimulus Saliency? J. Neurophysiol. 100, 815–828. https://doi.org/10.1152/jn.00097.2008

Iannetti, G.D., Zambreanu, L., Cruccu, G., Tracey, I., 2005. Operculoinsular cortex encodes pain intensity at the earliest stages of cortical processing as indicated by amplitude of laser-evoked potentials in humans. Neuroscience 131, 199–208. https://doi.org/10.1016/j.neuroscience.2004.10.035

Ishibashi, H., Tobimatsu, S., Shigeto, H., Morioka, T., Yamamoto, T., Fukui, M., 2000. Differential interaction of somatosensory inputs in the human primary sensory cortex: a magnetoencephalographic study. Clin. Neurophysiol. 111, 1095–1102. https://doi.org/10.1016/S1388-2457(00)00266-2

Jin, Q.Q., Wu, G.Q., Peng, W.W., Xia, X.L., Hu, L., Iannetti, G.D., 2018. Somatotopic Representation of Second Pain in the Primary Somatosensory Cortex of Humans and Rodents. J. Neurosci. 38, 5538–5550. https://doi.org/10.1523/JNEUROSCI.3654-17.2018

Jones, E.G., Wise, S.P., Coulter, J.D., 1979. Differential thalamic relationships of sensory-motor and parietal cortical fields in monkeys. J. Comp. Neurol. 183, 833–881. https://doi.org/10.1002/cne.901830410

Jones, S.R., Pritchett, D.L., Sikora, M.A., Stufflebeam, S.M., Hämäläinen, M., Moore, C.I., 2009. Quantitative Analysis and Biophysically Realistic Neural Modeling of the MEG Mu Rhythm: Rhythmogenesis and Modulation of Sensory-Evoked Responses. J. Neurophysiol. 102, 3554–3572. https://doi.org/10.1152/jn.00535.2009

Jones, S.R., Pritchett, D.L., Stufflebeam, S.M., Hamalainen, M., Moore, C.I., 2007. Neural Correlates of Tactile Detection: A Combined Magnetoencephalography and Biophysically Based Computational Modeling Study. J. Neurosci. 27, 10751–10764. https://doi.org/10.1523/JNEUROSCI.0482-07.2007

Kakigi, R., Inui, K., Tamura, Y., 2005. Electrophysiological studies on human pain perception. Clin. Neurophysiol. 116, 743–763. https://doi.org/10.1016/j.clinph.2004.11.016

Kanno, A., Nakasato, N., Hatanaka, K., Yoshimoto, T., 2003. Ipsilateral Area 3b Responses to Median Nerve Somatosensory Stimulation. NeuroImage 18, 169–177. https://doi.org/10.1006/nimg.2002.1283

Kenshalo, D.R., Iwata, K., Sholas, M., Thomas, D.A., 2000. Response Properties and Organization of Nociceptive Neurons in Area 1 of Monkey Primary Somatosensory Cortex. J. Neurophysiol. 84, 719–729. https://doi.org/10.1152/jn.2000.84.2.719

Lamour, Y., Willer, J.C., Guilbaud, G., 1983. Rat somatosensory (SmI) cortex: I. Characteristics of neuronal responses to noxious stimulation and comparison with responses to non-noxious stimulation. Exp. Brain Res. 49, 35–45. https://doi.org/10.1007/BF00235539

Law, R.G., Pugliese, S., Shin, H., Sliva, D.D., Lee, S., Neymotin, S., Moore, C., Jones, S.R., 2021. Thalamocortical mechanisms regulating the relationship between transient beta events and human tactile perception. bioRxiv 2021.04.16.440210. https://doi.org/10.1101/2021.04.16.440210

Lenoir, C., Huang, G., Vandermeeren, Y., Hatem, S.M., Mouraux, A., 2017. Human primary somatosensory cortex is differentially involved in vibrotaction and nociception. J. Neurophysiol. 118, 317–330. https://doi.org/10.1152/jn.00615.2016

Levitt, J., Edhi, M.M., Thorpe, R.V., Leung, J.W., Michishita, M., Koyama, S., Yoshikawa, S., Scarfo, K.A., Carayannopoulos, A.G., Gu, W., Srivastava, K.H., Clark, B.A., Esteller, R., Borton, D.A., Jones, S.R., Saab, C.Y., 2020. Pain phenotypes classified by machine learning using electroencephalography features. NeuroImage 223, 117256. https://doi.org/10.1016/j.neuroimage.2020.117256

Lin, Y.-Y., Chen, W.-T., Liao, K.-K., Yeh, T.-C., Wu, Z.-A., Ho, L.-T., Lee, L.-S., 2005. Differential generators for N20m and P35m responses to median nerve stimulation. NeuroImage 25, 1090–1099. https://doi.org/10.1016/j.neuroimage.2004.12.047

Lin, Y.-Y., Shih, Y.-H., Chen, J.-T., Hsieh, J.-C., Yeh, T.-C., Liao, K.-K., Kao, C.-D., Lin, K.-P., Wu, Z.-A., Ho, L.-T., 2003. Differential effects of stimulus intensity on peripheral and neuromagnetic cortical responses to median nerve stimulation. NeuroImage 20, 909–917. https://doi.org/10.1016/S1053-8119(03)00387-2

Lipton, M.L., Fu, K.-M.G., Branch, C.A., Schroeder, C.E., 2006. Ipsilateral Hand Input to Area 3b Revealed by Converging Hemodynamic and Electrophysiological Analyses in Macaque Monkeys. J. Neurosci. 26, 180–185. https://doi.org/10.1523/JNEUROSCI.1073-05.2006

Monconduit, L., Bourgeais, L., Bernard, J.-F., Bars, D.L., Villanueva, L., 1999. Ventromedial Thalamic Neurons Convey Nociceptive Signals from the Whole Body Surface to the Dorsolateral Neocortex. J. Neurosci. 19, 9063–9072. https://doi.org/10.1523/JNEUROSCI.19-20-09063.1999

Monconduit, L., Bourgeais, L., Bernard, J.-F., Villanueva, L., 2003. Convergence of cutaneous, muscular and visceral noxious inputs onto ventromedial thalamic neurons in the rat. PAIN® 103, 83–91. https://doi.org/10.1016/s0304-3959(02)00418-9

Mouraux, A., Iannetti, G.D., 2009. Nociceptive Laser-Evoked Brain Potentials Do Not Reflect Nociceptive-Specific Neural Activity. J. Neurophysiol. 101, 3258–3269. https://doi.org/10.1152/jn.91181.2008

Murakami, S., Okada, Y., 2006. Contributions of principal neocortical neurons to magnetoencephalography and electroencephalography signals. J. Physiol. 575, 925–936. https://doi.org/10.1113/jphysiol.2006.105379

Næss, S., Halnes, G., Hagen, E., Hagler, D.J., Dale, A.M., Einevoll, G.T., Ness, T.V., 2021. Biophysically detailed forward modeling of the neural origin of EEG and MEG signals. NeuroImage 225, 117467. https://doi.org/10.1016/j.neuroimage.2020.117467

Neymotin, S.A., Daniels, D.S., Caldwell, B., McDougal, R.A., Carnevale, N.T., Jas, M., Moore, C.I., Hines, M.L., Hämäläinen, M., Jones, S.R., 2020. Human Neocortical Neurosolver (HNN), a new software tool for interpreting the cellular and network origin of human MEG/EEG data. eLife 9, e51214. https://doi.org/10.7554/eLife.51214

Okada, Y.C., Wu, J., Kyuhou, S., 1997. Genesis of MEG signals in a mammalian CNS structure. Electroencephalogr. Clin. Neurophysiol. 103, 474–485. https://doi.org/10.1016/S0013-4694(97)00043-6

Omori, S., Isose, S., Otsuru, N., Nishihara, M., Kuwabara, S., Inui, K., Kakigi, R., 2013. Somatotopic representation of pain in the primary somatosensory cortex (S1) in humans. Clin. Neurophysiol. 124, 1422–1430. https://doi.org/10.1016/j.clinph.2013.01.006

Peng, W., Xia, X., Yi, M., Huang, G., Zhang, Z., Iannetti, G., Hu, L., 2018. Brain oscillations reflecting pain-related behavior in freely moving rats. PAIN 159, 106–118. https://doi.org/10.1097/j.pain.0000000000001069

Peterson, N.N., Schroeder, C.E., Arezzo, J.C., 1995. Neural generators of early cortical somatosensory evoked potentials in the awake monkey. Electroencephalogr. Clin. Neurophysiol. Potentials Sect. 96, 248–260. https://doi.org/10.1016/0168-5597(95)00006-E

Ploner, M., Schmitz, F., Freund, H.-J., Schnitzler, A., 1999. Parallel Activation of Primary and Secondary Somatosensory Cortices in Human Pain Processing. J. Neurophysiol. 81, 3100–3104. https://doi.org/10.1152/jn.1999.81.6.3100

Qiu, Y., Noguchi, Y., Honda, M., Nakata, H., Tamura, Y., Tanaka, S., Sadato, N., Wang, X., Inui, K., Kakigi, R., 2006. Brain Processing of the Signals Ascending Through Unmyelinated C Fibers in Humans: An Event-Related Functional Magnetic Resonance Imaging Study. Cereb. Cortex 16, 1289–1295. https://doi.org/10.1093/cercor/bhj071

Raij, T.T., Vartiainen, N.V., Jousmäki, V., Hari, R., 2003. Effects of Interstimulus Interval on Cortical Responses to Painful Laser Stimulation. J. Clin. Neurophysiol. 20, 73–79.

Schlereth, T., Baumgärtner, U., Magerl, W., Stoeter, P., Treede, R.-D., 2003. Left-hemisphere dominance in early nociceptive processing in the human parasylvian cortex. NeuroImage 20, 441–454. https://doi.org/10.1016/S1053-8119(03)00345-8

Schroeder, C.E., Seto, S., Arezzo, J.C., Garraghty, P.E., 1995. Electrophysiological evidence for overlapping dominant and latent inputs to somatosensory cortex in squirrel monkeys. J. Neurophysiol. 74, 722–732. https://doi.org/10.1152/jn.1995.74.2.722

Sliva, D.D., Black, C.J., Bowary, P., Agrawal, U., Santoyo, J.F., Philip, N.S., Greenberg, B.D., Moore, C.I., Jones, S.R., 2018. A Prospective Study of the Impact of Transcranial Alternating Current Stimulation on EEG Correlates of Somatosensory Perception. Front. Psychol. 9, 2117. https://doi.org/10.3389/fpsyg.2018.02117

Sorrentino, A., Parkkonen, L., Pascarella, A., Campi, C., Piana, M., 2009. Dynamical MEG source modeling with multi-target Bayesian filtering. Hum. Brain Mapp. 30, 1911–1921. https://doi.org/10.1002/hbm.20786

Tan, L.L., Oswald, M.J., Heinl, C., Retana Romero, O.A., Kaushalya, S.K., Monyer, H., Kuner, R., 2019. Gamma oscillations in somatosensory cortex recruit prefrontal and descending serotonergic pathways in aversion and nociception. Nat. Commun. 10, 983. https://doi.org/10.1038/s41467-019-

08873-z
Tiesinga, P., Sejnowski, T.J., 2009. Cortical Enlightenment: Are Attentional Gamma Oscillations Driven by ING or PING? Neuron 63, 727–732. https://doi.org/10.1016/j.neuron.2009.09.009
Tiihonen, J., Hari, R., Hämäläinen, M., 1989. Early deflections of cerebral magnetic responses to median nerve stimulation. Electroencephalogr. Clin. Neurophysiol. Potentials Sect. 74, 290–296. https://doi.org/10.1016/0168-5597(89)90059-2
Timmermann, L., Ploner, M., Haucke, K., Schmitz, F., Baltissen, R., Schnitzler, A., 2001. Differential Coding of Pain Intensity in the Human Primary and Secondary Somatosensory Cortex. J. Neurophysiol. 86, 1499–1503. https://doi.org/10.1152/jn.2001.86.3.1499
Treede, R.-D., Kenshalo, D.R., Gracely, R.H., Jones, A.K.P., 1999. The cortical representation of pain. PAIN 79, 105–111. https://doi.org/10.1016/S0304-3959(98)00184-5
Treede, R.-D., Kief, S., Hölzer, T., Bromm, B., 1988. Late somatosensory evoked cerebral potentials in response to cutaneous heat stimuli. Electroencephalogr. Clin. Neurophysiol. 70, 429–441. https://doi.org/10.1016/0013-4694(88)90020-X
Treede, R.-D., Lorenz, J., Baumgärtner, U., 2003. Clinical usefulness of laser-evoked potentials. Neurophysiol. Clin. Neurophysiol. 33, 303–314. https://doi.org/10.1016/j.neucli.2003.10.009
Treede, R.D., Meyer, R.A., Raja, S.N., Campbell, J.N., 1995. Evidence for two different heat transduction mechanisms in nociceptive primary afferents innervating monkey skin. J. Physiol. 483, 747–758. https://doi.org/10.1113/jphysiol.1995.sp020619
Valentini, E., Hu, L., Chakrabarti, B., Hu, Y., Aglioti, S.M., Iannetti, G.D., 2012. The primary somatosensory cortex largely contributes to the early part of the cortical response elicited by nociceptive stimuli. NeuroImage 59, 1571–1581. https://doi.org/10.1016/j.neuroimage.2011.08.069
Vierck, C.J., Whitsel, B.L., Favorov, O.V., Brown, A.W., Tommerdahl, M., 2013. Role of primary somatosensory cortex in the coding of pain. PAIN® 154, 334–344. https://doi.org/10.1016/j.pain.2012.10.021
Wang, X.-J., Buzsáki, G., 1996. Gamma Oscillation by Synaptic Inhibition in a Hippocampal Interneuronal Network Model. J. Neurosci. 16, 6402–6413. https://doi.org/10.1523/JNEUROSCI.16-20-06402.1996
Whitsel, B.L., Favorov, O.V., Li, Y., Lee, J., Quibrera, P.M., Tommerdahl, M., 2010. Nociceptive Afferent Activity Alters the SI RA Neuron Response to Mechanical Skin Stimulation. Cereb. Cortex 20, 2900–2915. https://doi.org/10.1093/cercor/bhq039
Wikström, H., Huttunen, J., Korvenoja, A., Virtanen, J., Salonen, O., Aronen, H., Ilmoniemi, R.J., 1996. Effects of interstimulus interval on somatosensory evoked magnetic fields (SEFs): a hypothesis concerning SEF generation at the primary sensorimotor cortex. Electroencephalogr. Clin. Neurophysiol. Potentials Sect. 100, 479–487. https://doi.org/10.1016/S0168-5597(96)95688-9
Willis, W.D., 2007. The somatosensory system, with emphasis on structures important for pain. Brain Res. Rev., A Century of Neuroscience Discovery: Reflecting on the Nobel Prize to Golgi and Cajal in 1906 55, 297–313. https://doi.org/10.1016/j.brainresrev.2007.05.010
Willis, W.D., 1985. Pain pathways in the primate. Prog. Clin. Biol. Res. 176, 117–133.
Yamada, T., Kayamori, R., Kimura, J., Beck, D.O., 1984. Topography of somatosensory evoked potentials after stimulation of the median nerve. Electroencephalogr. Clin. Neurophysiol. Potentials Sect. 59, 29–43. https://doi.org/10.1016/0168-5597(84)90018-2
Yue, L., Iannetti, G.D., Hu, L., 2020. The Neural Origin of Nociceptive-Induced Gamma-Band Oscillations. J. Neurosci. 40, 3478–3490. https://doi.org/10.1523/JNEUROSCI.0255-20.2020
Zhang, Z.G., Hu, L., Hung, Y.S., Mouraux, A., Iannetti, G.D., 2012. Gamma-Band Oscillations in the Primary Somatosensory Cortex—A Direct and Obligatory Correlate of Subjective Pain Intensity. J. Neurosci. 32, 7429–7438. https://doi.org/10.1523/JNEUROSCI.5877-11.2012
Ziegler, D.A., Pritchett, D.L., Hosseini-Varnamkhasti, P., Corkin, S., Hämäläinen, M., Moore, C.I., Jones, S.R., 2010. Transformations in oscillatory activity and evoked responses in primary somatosensory cortex in middle age: A combined computational neural modeling and MEG study. NeuroImage, Computational Models of the Brain 52, 897–912. https://doi.org/10.1016/j.neuroimage.2010.02.004

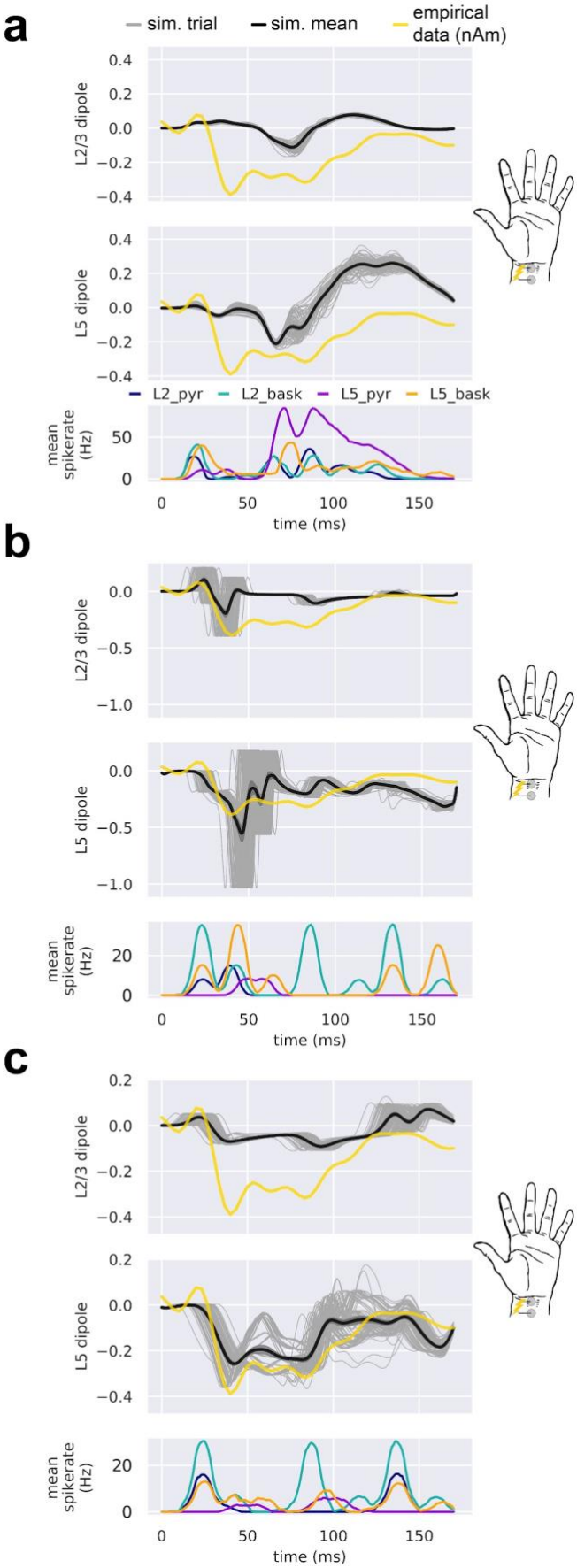

Supplementary Figure 1. Pyramidal neurons from L2/3 and L5 contribute differently to the simulated current dipole of the MN response. From top to bottom, each panel contains the simulated dipole (individual trials, grey traces n=100; trial-mean, black

trace) from L2/3 pyramidal neurons alongside the empirical MN response (yellow trace), the simulated dipole from L5 pyramidal neurons, and the population-mean spikerate (i.e., the average spikerate of a neuron of a given type). Panels (a-c) correspond to Figure 5a-c.

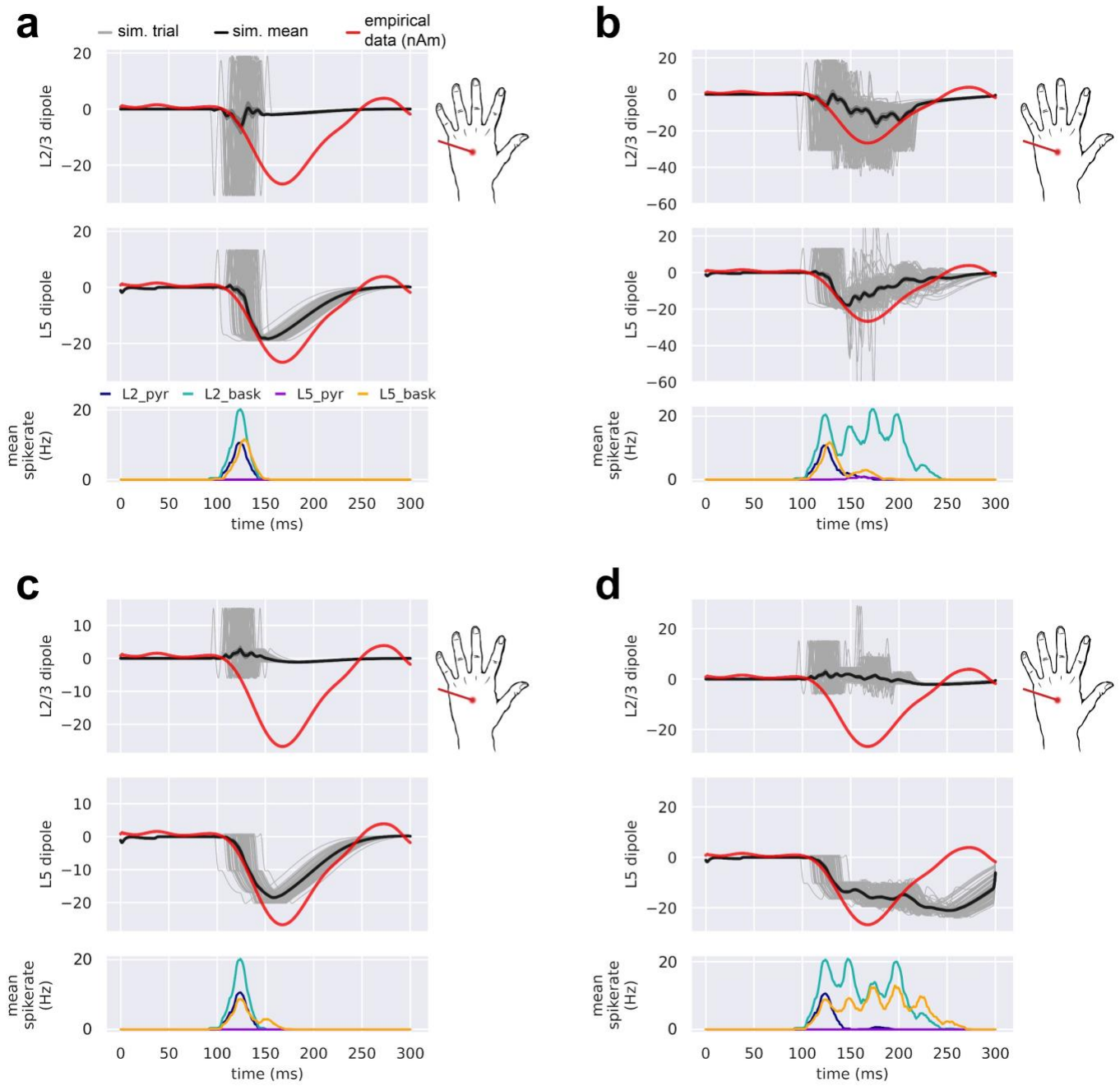

Supplementary Figure 2. Pyramidal neurons from L2/3 and L5 contribute differently to the manually-tuned simulated current dipole of the LE response. From top to bottom, each panel contains the simulated dipole (individual trials, grey traces n=100; trial-mean, black trace) from L2/3 pyramidal neurons alongside the empirical LE response (red trace), the simulated dipole from L5 pyramidal neurons, and the population-mean spikerate (i.e., the average spikerate of a neuron of a given type). Panels (a-c) correspond, respectively, to Figure 7a-c.

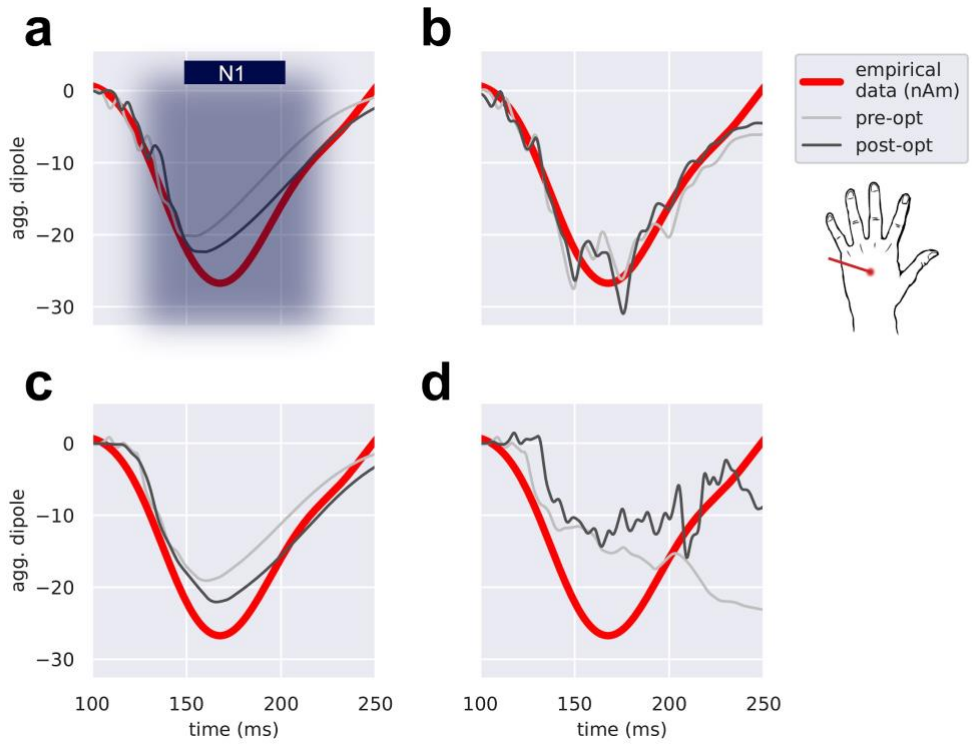

Supplementary Figure 3. Parameter optimization provides minimal improvement to the manually-tuned drive configurations shown in Figure 7. Except for the case with repetitive distal drives (b), the trial-average aggregate current dipole before (pre-opt, grey) and after (post-opt, black) optimization for all other drive configurations including a single distal drive (a), a single proximal drive (c), and repetitive proximal drives (d) fail to simulate the depth and breadth of the empirical LE N1 deflection (red).

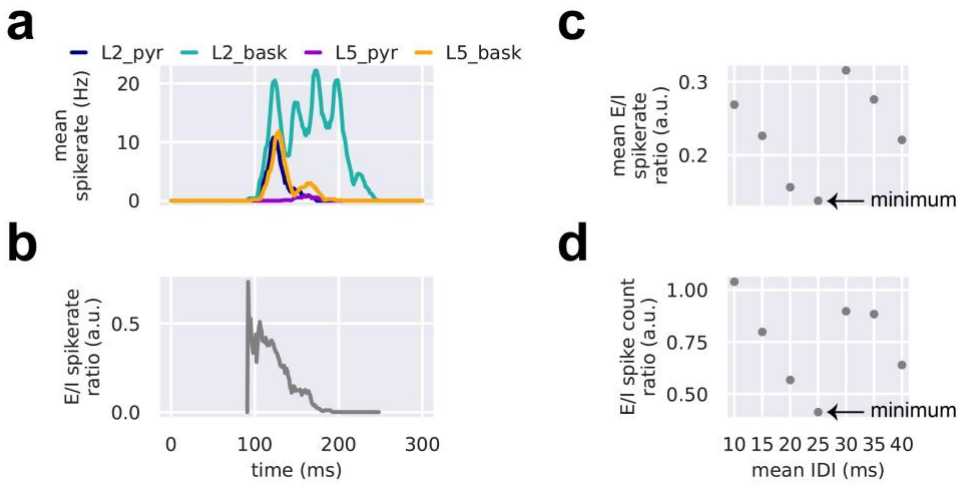

Supplementary Figure 4. A burst of repetitive distal drives delivered at mean intervals of 25 ms minimizes network excitation relative to network inhibition. Such an excitation/inhibition (E/I) balance maximizes downward current flow in the pyramidal apical dendrites while preventing runaway excitation. (a) With a mean 25 ms inter-drive-interval (IDI), repetitive distal drives recruit large amounts of L2/3 inhibitory basket cell spiking at corresponding intervals while largely diminishing the spikerate of other (i.e., L2/3 pyramidal, L5 pyramidal, and L5 basket) cell populations. (b) Also with a mean 25 ms IDI, the ratio of the aggregate mean excitatory (L2/3 + L5 pyramidal) cell spikerate divided by inhibitory (L2/3 + L5 basket) cell spikerate is always less than 1 and attenuates with successive distal drives from 120-195 ms. (c) Across simulations with mean IDIs ranging from 10-40 ms, the time-average E/I spikerate ratio is minimal with an IDI of 25 ms. (d) Same as (c), except instead of mean E/I spikerate ratio, we show the total E/I spike count ratio across all cells, all trials, and all time of the simulation.

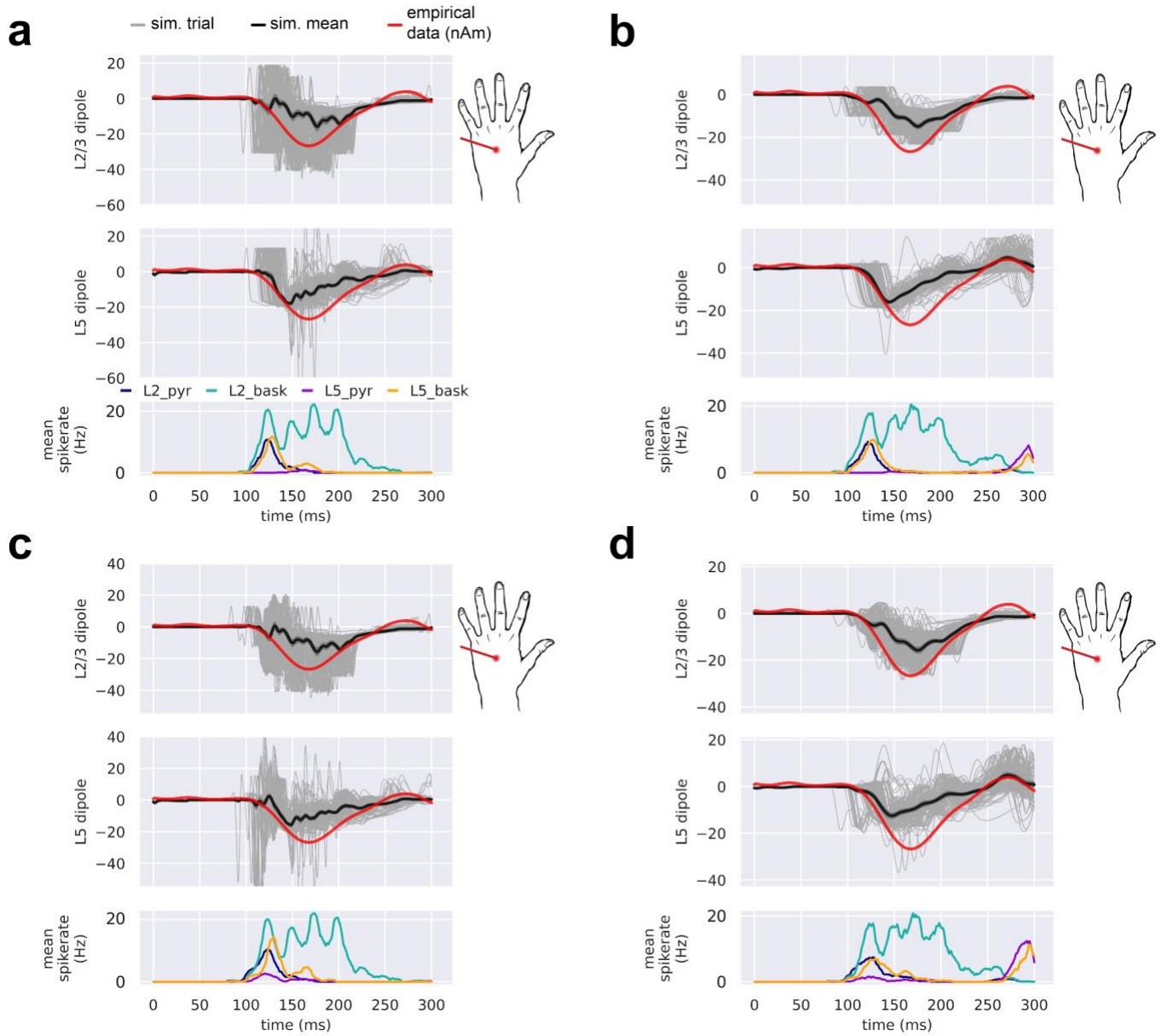

Supplementary Figure 5. Pyramidal neurons from L2/3 and L5 contribute differently to the optimized simulated current dipole of the LE response. From top to bottom, each panel contains the simulated dipole (individual trials, grey traces n=100; trial-mean, black trace) from L2/3 pyramidal neurons alongside the empirical LE response (red trace), the simulated dipole from L5 pyramidal neurons, and the population-mean spikerate (i.e., the average spikerate of a neuron of a given type). Panels (a-c) correspond, respectively, to Figure 9a-c.